Generative geomodelling: Deep Learning vs. Geostatistics

Suihong Song[1,*], Jiayuan Huang[1], Tapan Mukerji[1]

[1] Stanford University, 367 Panama St, Stanford, CA 94305, USA

Corresponding author: Suihong Song (suihong@stanford.edu)

Abstract

Generative geomodelling aims to simulate subsurface facies distributions while honoring multiple types of conditioning data and geological knowledge. This study selects three typical multiple-point statistics (MPS) approaches—Direct Sampling (DS), Quick Sampling (QS), and SNESIM—and two Generative Adversarial Network (GAN) workflows—post-GANs perturbation and GANSim—as representatives to compare traditional geostatistics-based and deep learning-based generative geomodelling methods, based on two sedimentary reservoir scenarios. In addition to the latest GANSim enhancements—namely, the local discriminator and facies-indicator output designs—this paper further proposes injecting global feature information into intermediate layers of the generator, instead of concatenating global features with latent vectors, to improve constraint effectiveness. The geomodelling results demonstrate that GANs, especially GANSim, consistently produce geologically realistic and diverse facies models that are accurately conditioned to well facies data, global features, and facies probability maps. In comparison, MPS approaches perform well in honoring well facies and probability maps but produce facies models with significantly lower geological realism. Their conditioning effectiveness on global features is also less reliable. GANSim achieves geomodelling speeds hundreds of times faster than MPS methods. Flow simulations show that GANSim results yield more accurate and less uncertain predictions than MPS outputs. Moreover, although trained on stationary conceptual geomodels, the trained GANSim generalizes well to model large, nonstationary reservoirs by spatially varying the input global feature maps and carefully designing the conditioning probability maps, making it a powerful and flexible tool for high-fidelity conditional geomodelling.

Key Words:

Generative geomodelling, Multiple-point statistics (MPS), Generative Adversarial Networks (GANs), GANSim, Non-stationarity

1 Introduction

Geomodelling, i.e., integrating various sources of data to characterize the spatial distribution of subsurface lithologies and petrophysical properties, is an essential step for successful exploitation of subsurface resources including minerals, hydrocarbon, hydrogen, geothermal, and underground water as well as for the secure geological storage of CO2.

To increase the accuracy of geomodelling, as many types of data or information as possible are fed into the geomodelling process, which may include sparsely distributed well interpretations of facies, three- or two-dimensional geophysical data, temporal dynamic data observed at wells (e.g., bottom-hole pressure change data), and geological knowledge about the subsurface. The simulated geomodels are expected to be consistent with all the aforementioned data and knowledge. Compared to the extremely high dimensionality of geomodels, data and knowledge always appear insufficient, so uncertainty quantification is critical in the geomodelling process. Consequently, multiple geomodel realizations are often produced to represent the uncertainty space of the earth models.

With traditional geostatistics-based geomodelling workflows, the former three types of data (i.e., well facies data, geophysical data, and temporal dynamic data) can be honored, through either a direct conditioning or an inversion method. With the direct conditioning approach, the well facies data and geophysics-interpreted facies probability maps are directly taken into geomodelling algorithms such as the variogram-based or multiple-point statistics-based methods to produce conditional geomodel realizations (Avseth et al., 2005; Azevedo & Soares, 2017; Doyen, 1988; Pyrcz & Deutsch, 2014). With the inversion method, an initial geomodel is iteratively perturbed in a manner consistent with the spatial geological structure to honor the given geophysical data or the dynamic data (Bortoli et al., 1993; Bosch, 1999; Bosch et al., 2010; Buland et al., 2008; Caers, 2003; Deutsch, 1992; Doyen, 2007; De Figueiredo et al., 2018; González et al., 2008; Grana et al., 2021; Haas & Dubrule, 1994; Hu, 2000).

Due to the often qualitative definition of geological knowledge and limitations of different geomodelling algorithms, geological knowledge may be represented in different forms and with different levels of completeness in different geomodelling algorithms: in the variogram-based and the multiple-point statistics (MPS)-based methods, geological knowledge is expressed as variograms and training images, respectively; in process-mimicking methods (e.g., ALLUVSIM by Pyrcz et al. (2009), Meanderpy by Sylvester et al. (2011), PB-SAND by Yan et al. (2017), the turbidite channels simulated in McHargue et al. (2011), and FLUMY by MINES PARIS PSL) and object-based methods, geological knowledge is expressed as rules, such as the shape of a crevasse splay or how a meandering channel evolves; and in process-based (or physics-based) methods, geological knowledge is approximated by physical equations that govern geological processes such as sediment transport, erosion, and deposition (Karssenberg & Bridge, 2008; Sun et al., 2010; Wang et al., 2021). Problems arise with these traditional methods in either imperfect reproduction of geological realism (i.e., in variogram- and MPS-based methods) or imperfect conditioning effects (i.e., in object-based, process-mimicking, and process-based methods) (Pyrcz & Deutsch, 2014). Furthermore, a significant challenge of process-based methods lies in reconciling the complexity—and therefore the realism—of the model with the necessity for extended modeling durations to obtain appropriate stratigraphic representations, which in turn demands substantial computational resources.

In recent years, deep learning-based geomodeling approaches have gained momentum, as evidenced by various references (Chan & Elsheikh, 2019; Dupont et al., 2018; Federico & Durlofsky, 2024; Laloy et al., 2017, 2018; Lee et al., 2023; Mosser et al., 2020; Nesvold & Mukerji, 2021; Song et al., 2021b, 2022a, 2022b; Zhang et al., 2019). In these approaches, geological knowledge is represented by numerous conceptual models and is learned from these conceptual models by neural networks through deep generative workflows such as Generative Adversarial Networks (GANs; Goodfellow et al. (2014)), diffusion models (Ho et al., 2020), or Variational Auto Encoders (VAE; Kingma & Welling (2014)). Although diffusion models are receiving increasing research attention in geomodelling (Federico & Durlofsky, 2024; Lee et al., 2025; Xu et al., 2024), GANs-based geomodelling is the most researched and mature method for geomodelling, to date. Within GANs, the neural network responsible for learning geological pattern knowledge is called a generator; after training, the generator can produce realistic geomodels that are consistent with required geological patterns from random latent vectors. To allow the produced geomodel to also honor the other three types of data (i.e., well facies data, geophysical data, and temporal dynamic data), researchers have proposed a post-GANs inversion or “geomodel perturbation” workflow which is similar to the workflow used in traditional geostatistics-based geomodelling approaches, except that here they perturb or sample the input low-dimensional latent vector of the generator to achieve the perturbation of high-dimensional geomodels to ultimately match the given conditioning data (e.g., Laloy et al., 2018; Mo et al., 2020; Mosser et al., 2020; Nesvold & Mukerji, 2021; Zhang et al., 2019). However, any change to the conditioning data requires repeating of such perturbation/optimization or sampling process.

Song et al. (2021b, 2022a) proposed a GANs-based geomodelling workflow called GANSim, to achieve direct conditioning on well facies data, geophysics-interpreted facies probability maps, and global features such as facies proportion or channel direction. In GANSim, the generator simultaneously learns the conditioning rules (i.e., the conditioning relationship between the output reservoir geomodel and the input conditioning data) together with the geological knowledge. With the two types of knowledge, the trained generator can directly take any new given well facies data, probability maps, and global feature values to produce diverse, realistic, and conditional geomodels. GANSim has been applied in 3D field karst cave reservoirs (Song et al., 2022b), where a trained generator quickly produced 3D facies geomodels for arbitrarily large field reservoir domains. The perturbation process of input latent vector can be integrated into GANSim workflow to honor temporal dynamic data (Song et al., 2023), where a physics-informed neural operator can be trained for fast forward flow simulation (Song et al., 2025).

There was a problem in order versions of GANSim that the well facies data occupying single pixels horizontally may be overlooked by the discriminator, leading to severe local disconnections between given well facies data and surrounding regions with the same facies type. Extension of well facies from single pixel into multiple pixels (e.g., 4×4 pixels) was used to mitigate the problem (Song et al., 2021b, 2022b), but it introduces local artifacts and artificially reduces uncertainty around wells. Song et al. (2025) proposed the design of local discriminator to address the "single-pixel well facies overlook" issue. The output of the generator is also improved from one channel of facies model into multiple channels of facies indicators for better rationality. Supporting Information S1 shows more detail about these enhancements. Based on these enhancements, a field 3D deltaic reservoir was successfully modeled (Alqassab et al., 2024).

In this paper, in section 2, we will use two GANs-based geomodelling workflows (post-GANs and GANSim) and three typical MPS approaches as representatives to compare deep learning-based and geostatistics-based generative geomodelling methods, based on two sedimentary reservoir scenarios. The latest GANSim enhancements are considered, and another enhancement about the input pipeline of global features in the generator of GANSim is also proposed here. Then in Section 3, further in-depth discussions about the distribution relationship between GANs and MPS results and the simulation of nonstationary facies models are presented. Finally, conclusions will be drawn in Section 4.

2. Comparison of GANs with MPS in two reservoir scenarios

Both the post-GANs perturbation and GANSim workflows can be applied to condition on global features such as channel direction and facies proportion. In this section, first we compare the two GANs workflows with three typical MPS approaches—Direct Sampling (DS; Mariethoz et al. (2010)), Quick Sampling (QS; Gravey & Mariethoz (2020)), and SNESIM (Strebelle, 2002) embedded in Petrel software—in cases of only conditioning to global features based on two reservoir scenarios. There are slight differences among the three MPS approaches. SNESIM first scans the entire training image (TI) and organizes all events into a search tree; then, when simulating a point, a conditional probability function is calculated from the search tree to sample a facies code for that location. In DS and QS, each time a point is simulated, a similar event is directly searched from the TI, and the center facies code of the matched event is assigned to the simulation point. QS differs from DS mainly in that it uses fast Fourier transforms to compute the similarity between the event in the TI and the neighborhood around the simulation point. Then, the GANSim workflow and SNESIM are further compared in cases of conditioning to not only global features, but also well facies data, and facies probability maps. In summary, we compare two GANs workflows with DS, QS, and SNESIM for conditioning to global features. Then we compare GANSim and SNESIM for conditioning to global as well as local conditioning data. All this is done for two different reservoir scenarios.

The first reservoir scenario to be studied is fluvial channel sedimentary system. We use a dataset created by Song et al. (2021a), which includes 35,640 conceptual facies models (2D horizontal sections) each containing 64×64 cells representing an area of 3200×3200 m. There are three sedimentary facies types: sandy channel center facies, sandy channel levee facies, and inter-channel mud facies. Global features include channel direction, mud proportion, channel center width, channel amplitude, and channel wavelength. The channel direction, -90 to 90 degrees clockwise from the north direction, is equally divided into 30 categories, with each category corresponding to 6 degrees. The channel center width can be 27, 31, or 34 m with equal probability. The channel amplitude ranges from 7 to 111 m. The channel wavelength can be 100, 120, 140, or 160 m. The mud proportion ranges from 0.14 to 0.59. These conceptual geomodels are split into a training dataset having 32,640 geomodels and a test dataset having 3,000 geomodels. The second scenario is a meandering point bar sedimentary system. We use a dataset created by Hu et al. (2024). There are 11,785 conceptual facies models in the dataset, each containing 64×64 cells representing a domain of 640×640 m. Four sedimentary facies are considered: muddy floodplain, muddy channel fill, sandy lateral accretion, and mud drape. The latter two facies constitute a complete point bar geobody. Global features include floodplain proportion and point bar-to-channel fill ratio. The former varies from 0.42 to 0.81, while the latter varies from 0 to 2.2. The dataset is split into a training dataset with 10,000 facies models and a test dataset with 1,785 facies models. For each conceptual geomodel of the two datasets, a well facies data and a set of facies probability maps for all facies types are obtained by random sampling and smoothing with a Gaussian kernel. Each sampled well facies point occupies only one cell, and the well number is between 1 to 10 for each well facies data. See Figure 3 and Figure 4 for two examples of the two datasets.

2.1 Geomodelling conditioned to global features

According to the customary practices of MPS, the geomodelling process only involving a TI is called "unconditional geomodelling". However, since the TI has already embedded the concepts of global features, the simulated results may internally honor these global feature values. Therefore, in this paper, this process is called geomodelling conditioned to global features, in order to be consistent with GANs-based geomodelling terminology.

For the fluvial channel reservoir scenario, it is assumed that the geomodel realizations need to be conditioned to the following global features: the channel direction is 42 to 48 degrees clockwise from the north, which is within the direction category 22. The channel center width, channel amplitude, and channel wavelength are 31 m, 55 m, and 121 m, respectively. The mud proportion is 0.65. Following steps of the post-GANs inversion workflow, an unconditional generator is first trained, which takes 6 hours on one GPUs (A100). Then, a Markov chain Monte Carlo (McMC) Bayesian workflow is performed to sample appropriate input latent vectors of the trained unconditional generator that are consistent with the given conditioning global feature values (as above). Finally, 45,673 appropriate latent vectors and the same number of facies model realizations are obtained, with each latent vector taking 0.107 s on average. In the GANSim workflow, a generator conditioned to the five types of global features are trained, which takes 6 hours on one GPU (A100). Then, the conditioning global feature values are taken into the trained generator to produce multiple conditional realizations. The generation of each realization takes 0.3 ms on one GPU (A100) on average. Figure 1 shows several random results of both GANs workflows. Supporting Information S2 provides more details about the execution of the two workflows. It is worth noting that in the aforementioned McMC workflow, the global features of each facies model produced by the trained unconditional generator are obtained using an additionally trained recognizer neural network. The input pipeline of global features in the generator of GANSim is improved from the original design of concatenating global features with latent vectors into a new design of injecting global features into different middle neural network layers to strengthen the constraint effect of global features (see more detail in the Supporting Information S1).

MPS methods honor global features mainly through construction of TIs. Corresponding to the 5 given global feature values, a large 200×200-cell TI is first constructed (Figure 1) with the same method for the conceptual facies models. Then, the three MPS methods—DS, QS, and SNESIM—are used for geomodelling with that TI. Figure 1 shows random simulation results of these methods. The hyperparameters used in these methods and results of other hyperparameter settings are provided in more detail in Supporting Information S2. Some hyperparameter combinations can produce more realistic results, but there are clear tendencies to replicate the TI. Here, appropriate hyperparameter combinations are selected to balance the produced realism and repetition rate.

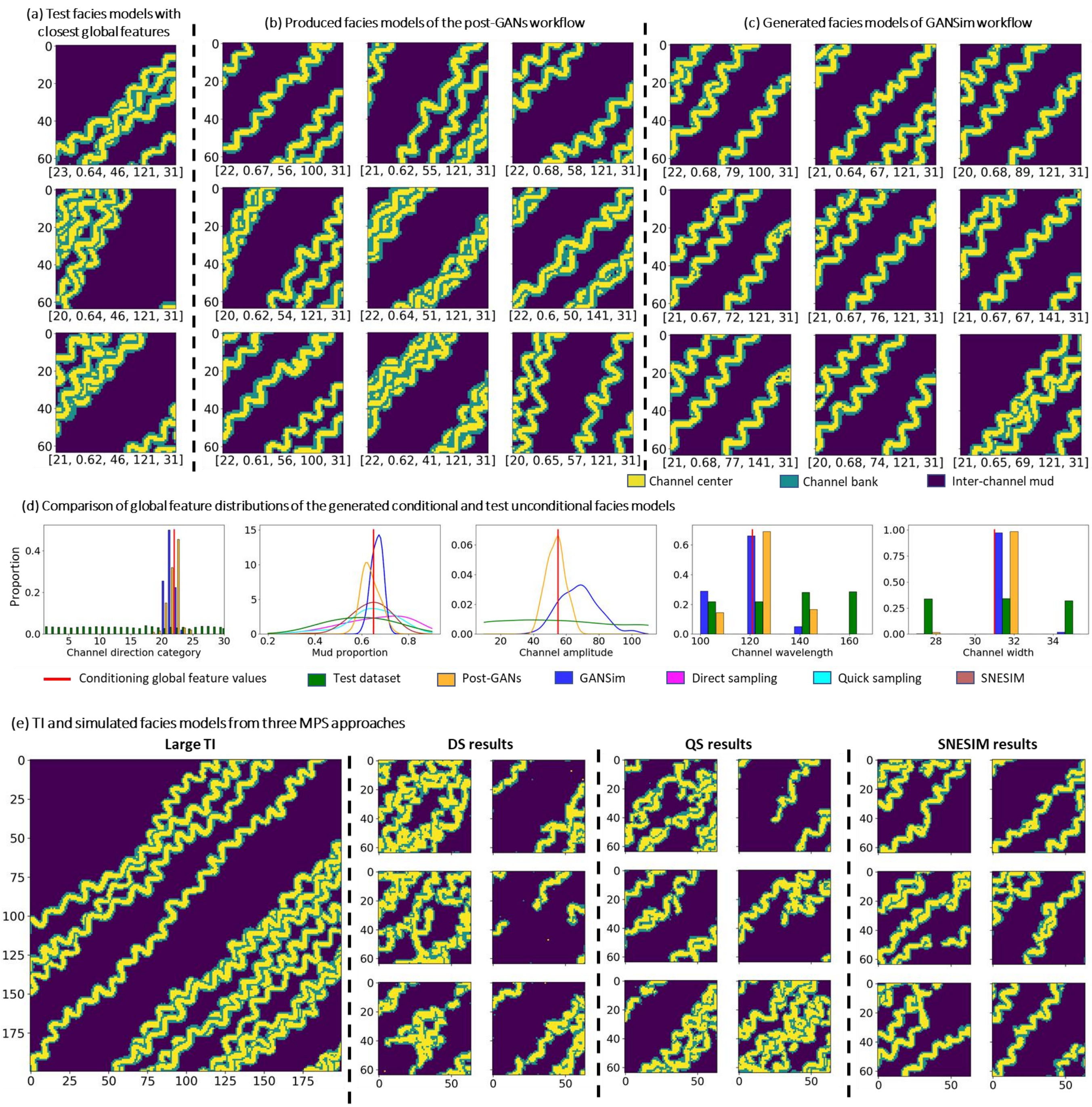

Figure 1. Comparison of geomodelling results of the two GANs workflows and the three MPS approaches in fluvial channel scenario. (a) Three test facies models with the closest global features to the given ones. (b) and (c) are random results of the two GANs workflows. The five values in the bracket below each facies model show the channel category, mud proportion, channel amplitude, channel wavelength, and channel center width of that facies model. (d) compares the global feature distributions measured from facies models resulting from the two GANs workflows and the three MPS approaches (only for mud proportion global feature). (e) shows the constructed TI and random simulation results of the three MPS approaches.

For the point bar reservoir scenario, the assumed conditioning global feature values are 0.74 for the floodplain proportion and 1.14 for the point bar-to-channel fill ratio. The same procedures as in the previous fluvial channel scenario are used here. Figure 2 compares simulated realizations GANs and MPS approaches. More detail about the execution of these approaches is provided in Supporting Information S3.

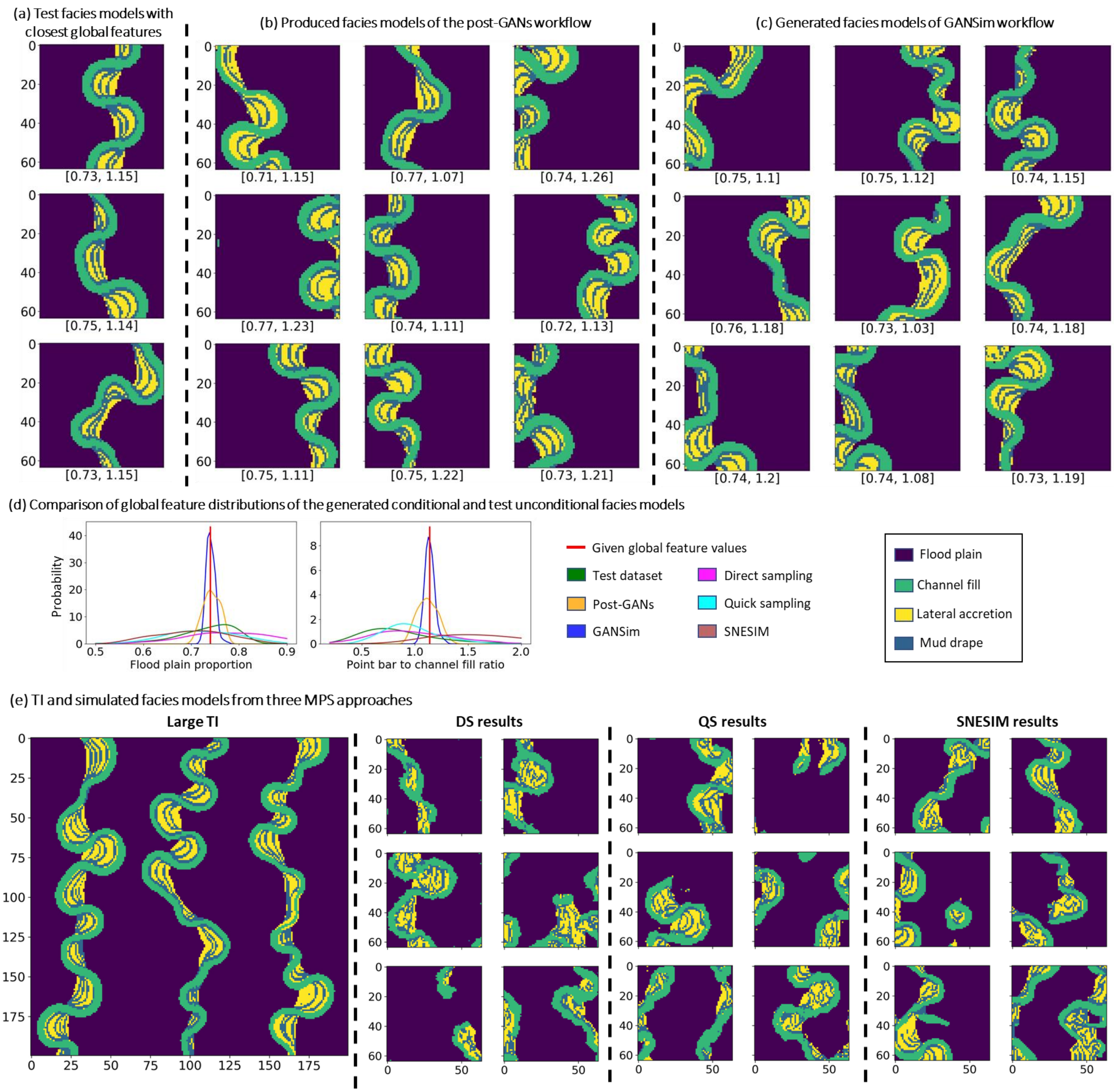

Figure 2. Comparison of geomodelling results of the two GANs workflows and the three MPS approaches in point bar scenario. (a) Three test facies models with the closest global features to the given ones. (b)

and (c) are random results of the two GANs workflows. The two values in the bracket below each facies model shows the corresponding floodplain proportion and point bar-to-channel fill ratio features. (d) compares the global feature distributions of facies models resulting from the two GANs and the three MPS approaches. (e) shows the constructed TI and the simulation results of the three MPS approaches.

It is clear from Figure 1 and Figure 2 that the results of both GANs workflows are realistic and diversified in both reservoir scenarios. The global feature histograms (or probability density functions) obtained from 200 realizations of both workflows indicate a close consistency between these realizations and the conditioning values, compared to test facies models. Note that an additional neural network is trained to specially recognize the global features for each generated facies model in the fluvial channel scenario. In comparison, the simulation results of the three MPS approaches are much worse in produced geological realism (e.g., shape, connection, and reciprocal relations of geobodies). Indeed, these MPS methods are able to produce good realism with appropriate hyperparameter settings, but there is a tendency of directly replicating from TIs, largely reducing the diversity of the simulated realizations (see Supporting Information S2 and S3 for detail). As to conditioning effects, due to the poor realism, it is challenging to quantitatively evaluate the geometrical global features including channel width, direction, wavelength, and amplitude of produced geomodels for the three MPS approaches, but the realizations “look” consistent with the TI. However, for other calculable features—mud proportion, floodplain proportion, and point bar-to-channel fill ratio—the probability density function curves derived from the realizations of the three MPS approaches are broadly distributed and do not exhibit a clear clustering tendency toward the conditioning values. The simulation of each geomodel takes 0.07 s, 0.3 s, and 0.3 s with DS, QS, and SNESIM algorithm on average in both scenarios. Note also that the MPS methods do not need prior training on GPUs but need a representative and large training image.

2.2 Geomodelling conditioned to global features, well facies data, and probability maps

We compare GANSim workflow with SNESIM in the two reservoir scenarios when conditioning to global features, well facies data, and probability maps. In each scenario, a generator conditioned to all the three types of conditioning data is trained. The probability maps of channel center and levee facies are considered in the fluvial channel scenario, while those of mud drape, channel fill, and lateral accretion facies are considered in the point bar scenario. The training takes 10 and 9 hours for the channel and point bar scenario, respectively, at two GPUs (A100). Once trained, any given conditioning data can be taken into the generator to produce different facies model realizations. To evaluate the trained generators, some test geomodels are taken as the reference, and their global features, well facies data, and facies probability maps are used as the conditioning data, as shown in Figure 3 and Figure 4. When simulating with SNESIM, a 200×200-cell TI is first constructed using the given global feature values. Then, multiple facies model realizations are simulated using that TI, the given well facies data, and the given probability maps. In the point bar scenario, the TI constructed in Section 2.1 (Figure 2) having almost the same global feature values as the reference geomodel is used. Random simulated facies model realizations of both GANSim and SNESIM are shown in Figure 3 and Figure 4. More detail is provided in Supporting Information S4. It is worth noting that the latest enhancements proposed by Song et al. (2025) are considered in the GANSim neural network architecture, including introduction of local discriminators and output of the generator as multiple facies indicators. The input global features are concatenated into different middle neural layers of the generator to strengthen constraint effect. See more detail in Supporting Information S1.

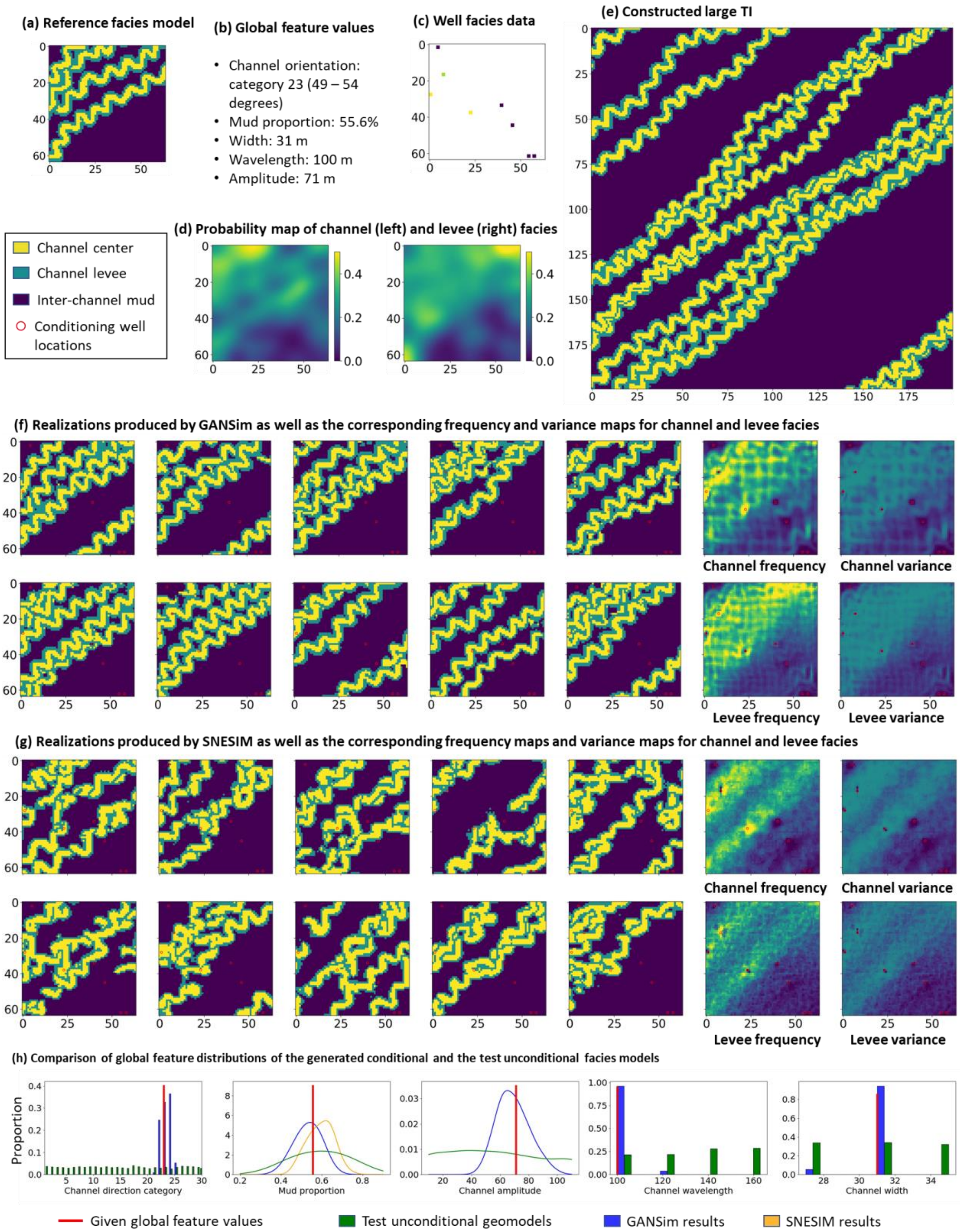

Figure 3. Comparison of conditional facies model realizations resulting from GANSim and DS in the fluvial channel reservoir scenario. The well points are expanded from 1x1-size area into 3x3-size area here only for better visualization.

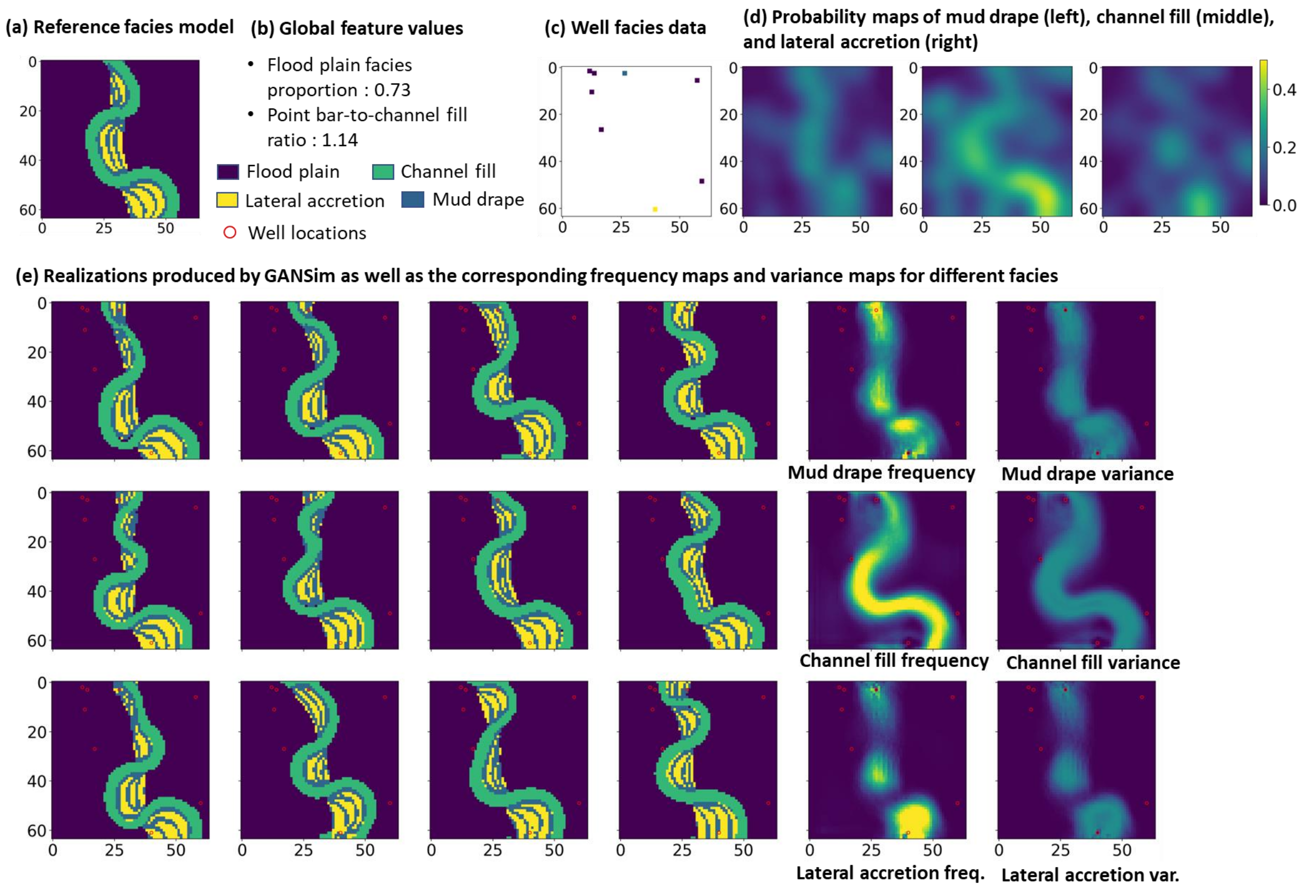
(a) Reference facies model
(b) Global feature values
Flood plain facies proportion : 0.73
Point bar-to-channel fill ratio : 1.14
Flood plain
Channel fill
Lateral accretion
Mud drape
Well locations
(c) Well facies data
(d) Probability maps of mud drape (left), channel fill (middle), and lateral accretion (right)
(e) Realizations produced by GANSim as well as the corresponding frequency maps and variance maps for different facies
Mud drape frequency
Mud drape variance
Channel fill frequency
Channel fill variance
Lateral accretion freq.
Lateral accretion var.

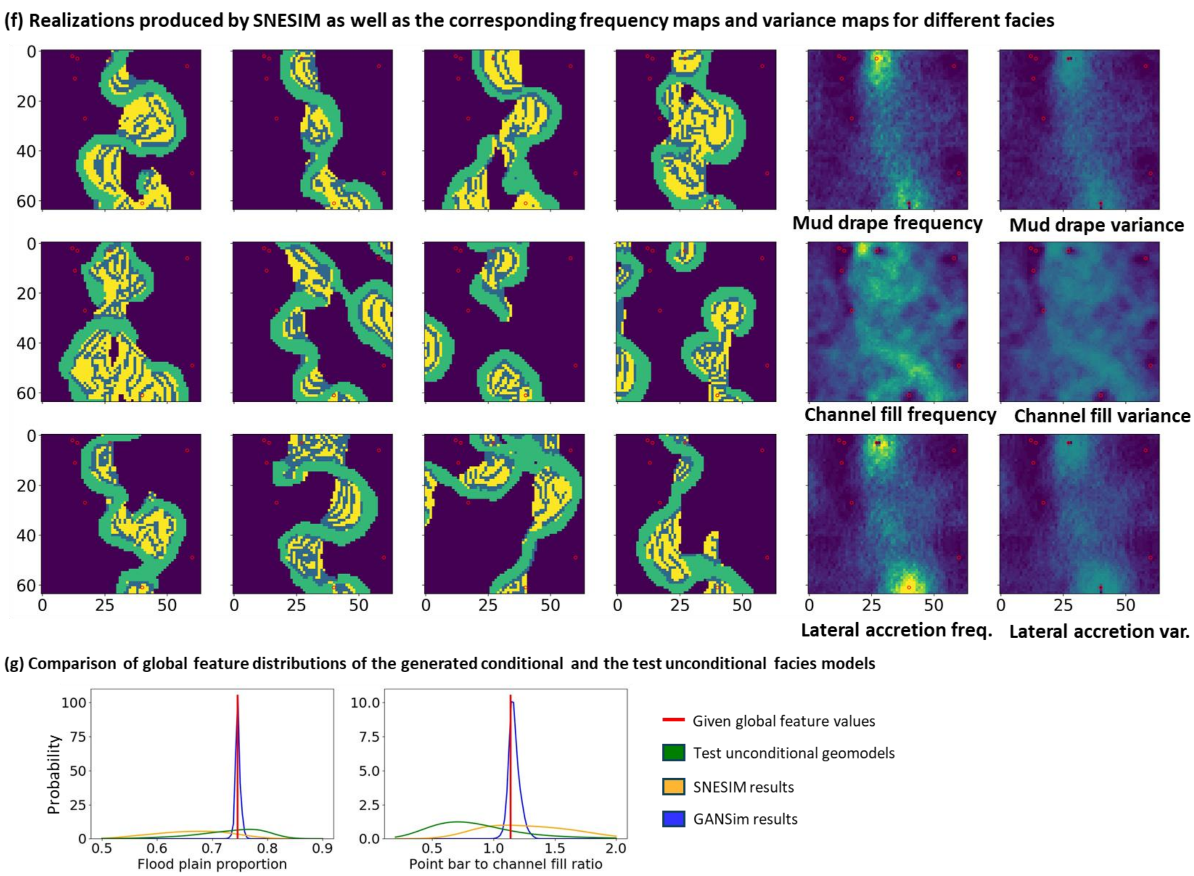

Figure 4. Comparison of conditional facies model realizations resulting from GANSim and SNESIM in the point bar reservoir scenario. The well points are expanded from 1x1-size area into 3x3-size area here only for better visualization.

It is clear from Figure 3 and Figure 4 that the GANSim-produced facies model realizations are realistic both globally and locally around well facies data, diversified, and consistent with all the conditioning data. Such consistency can be proved by the comparison between the global feature distributions of produced facies models and the input conditioning global feature values, the comparison between facies frequency maps and the input conditioning probability maps, and the fact that the well facies data reproduction accuracy being 100% in both scenarios. It is worth noting that the "single-pixel well facies overlook" issue and its consequence of local disconnection around wells in Song et al. (2021b) have been addressed by the enhanced GANSim architecture design (see Supporting Information S1). The SNESIM-produced facies model realizations also honor the given well facies data (with reproduction accuracy of 100%) and facies probability maps quite well, which is internally designed by the algorithm. However, the facies realizations are much less realistic than GANSim results. For the calculable global features of simulated realizations—mud proportion, floodplain proportion, and point bar-to-channel fill ratio, they may be close to the given conditioning values (mud proportion in channel scenario) or may not (the remaining two global features in point bar scenario). As for other geometrical global features, the produced realizations "look" consistent with the TIs, to some extent.

Is there significant difference in flow behavior when using GANSim- and MPS-produced facies models? To answer that question, a single-phase fluid flow simulation from the north to the south is conducted on the reference, 100 GANSim-produced and 100 SNESIM-produced geomodels of the two test cases (Figure 3 and Figure 4) in both scenarios. A commercial flow simulator, Eclipse, is used in this study. The north boundary, the south boundary, and the initial pressure values are fixed at 300, 250, and 250 bar. The permeability values for channel center, channel levee, and mud facies are set as 2500, 500, and 10 mD in the fluvial channel scenario. In the point bar scenario, the permeability values for sandy lateral accretion, channel fill, mud drape, and flood plain facies are set as 2200, 1500, 50, and 10 mD, respectively. Figure S4-1 and Figure S4-2 (in Supporting Information S4) shows pressure distribution maps after different days of flow simulation for the reference, 5 random GANSim-produced and 5 random SNESIM-produced geomodels of the two test cases. The flow results of GANSim-produced geomodels are much more similar to the flow results of the reference geomodel than the SNESIM-produced geomodels both in spatial patterns and magnitudes. The prediction of flow front is of great interest in many practical cases. Here, we assume the pressure of 255 bar as the flow front and calculate the probability map of being within the flow front—with pressure values larger than 255 bar—on different days after flowing from flow simulation results of the 100 GANSim- and the 100 SNESIM-produced geomodels (Figure 5). In the figure, the blue curves are contours of 95% and 5%, while the red curves represent the flow fronts of the reference geomodels. The areas between the 95% and 5% contours represent the predicted regions for flow fronts. We can see that although the predicted regions of GANSim and SNESIM both cover the reference front curves, the former are much narrower than the latter on different days, indicating a more accurate prediction with GANSim than SNESIM in flow behaviors and following decision-making processes.

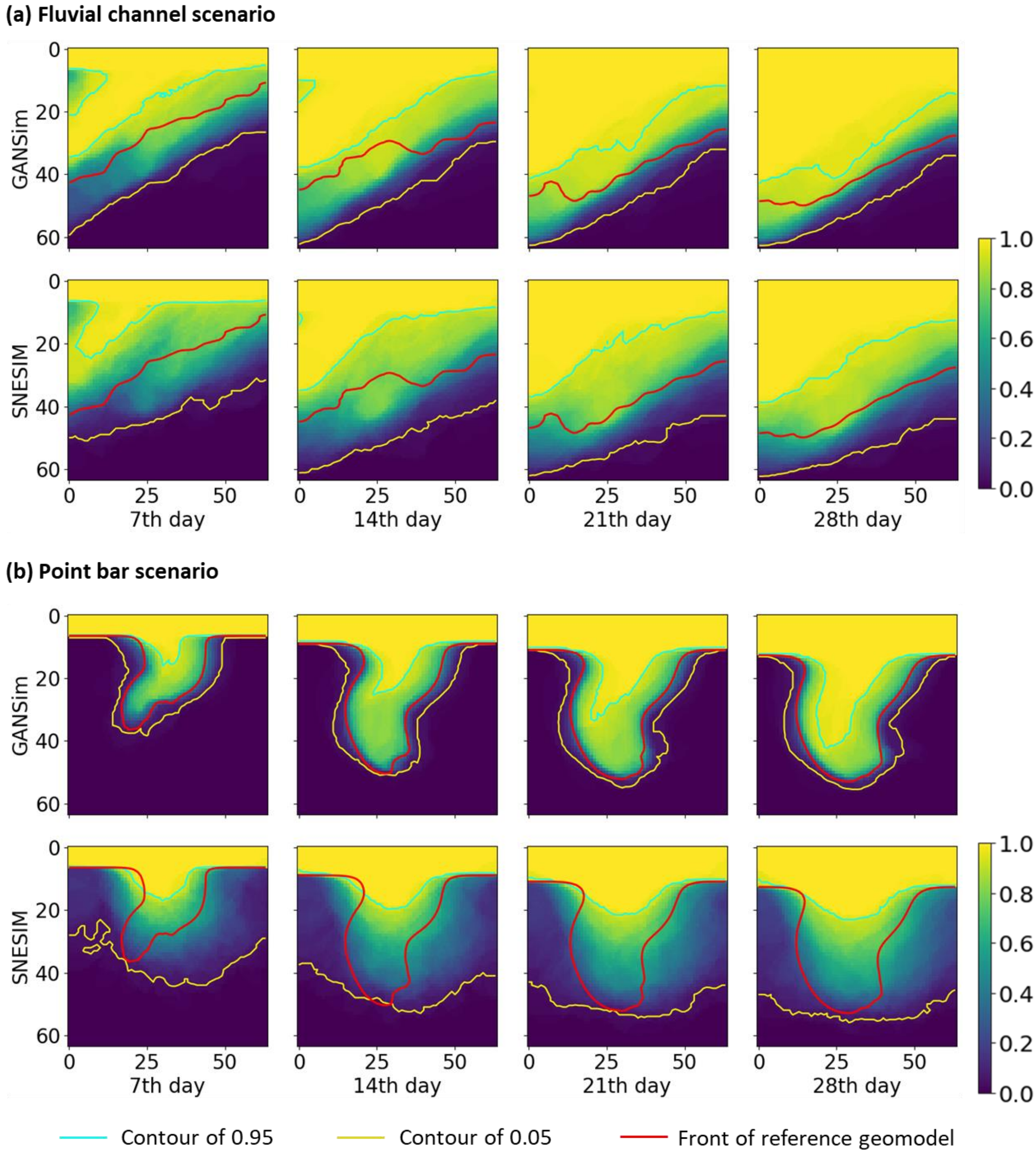

Figure 5. Probability maps of being within the flow front, $p(pressure > 255\ bar)$ on different days after flowing for GANSim and SNESIM in the two test cases of both scenarios.

3. Discussions

3.1 Comparison of distributions of GANs and MPS results

It is clear from the above results that GANs-produced geomodels have nearly the same level of realism as the test geomodels and the largest allowed degree of variation (see Figure S2-1, Figure S3-1, and Figure 1 - 4). MPS results are much worse in realism, albeit with good conditioning. Based on these observations and the theory of GANs that a generator would finally approximate the distribution of training samples (Goodfellow et al., 2014), a schematic diagram describing the distribution relationship among conceptual (training), GANs-produced, and MPS-produced geomodels is presumably concluded (Figure 6). In the unconditional case, the distribution of GANs results almost overlaps with that of conceptual geomodels, i.e., $p(m; GANs) \approx p(concpt.m)$, where m is a geomodel, and $concpt.m$ refers to the conceptual geomodel. It is worth noting that conceptual geomodels are essentially the samples of the geological pattern knowledge about the reservoir, thus $p(concpt.m) \approx p(m|geo.pat.)$, where $geo.pat.$ refers to the geological pattern knowledge used to construct conceptual geomodels.

With conditioning, the distribution of GANs outputs shrinks, but the GANs' adversarial loss continues to encourage the GANs output distribution to approach the conceptual geomodel distribution even under the circumstance of conditioning. Thus, $p(m|cond.; GANs) = p(m; GANs|cond.) \approx p(concpt.m|cond.) \approx p(m|geo.pat., cond.)$. Note that in geomodelling the requisite is lots of geomodels consistent with both geological pattern knowledge and conditioning data, i.e., $p(m|geo.pat., cond.)$. In comparison, MPS-produced geomodels honor given conditioning well facies and facies probability maps very well and have enough diversity, but the realism deteriorates, thus they may have a distribution shown by the blue contours on the surface of conditioning = 1. In MPS, the conditioning global features are embedded into TIs, so "*cond.*" in $p(m|TI., cond.; MPS)$ only includes well facies and probability maps, which is different from GANs where "*cond.*" includes all conditioning data. In some cases, MPS results may not honor the given global feature values (e.g., Figure 4), so the distribution of MPS results may shift away from the surface of conditioning = 1.

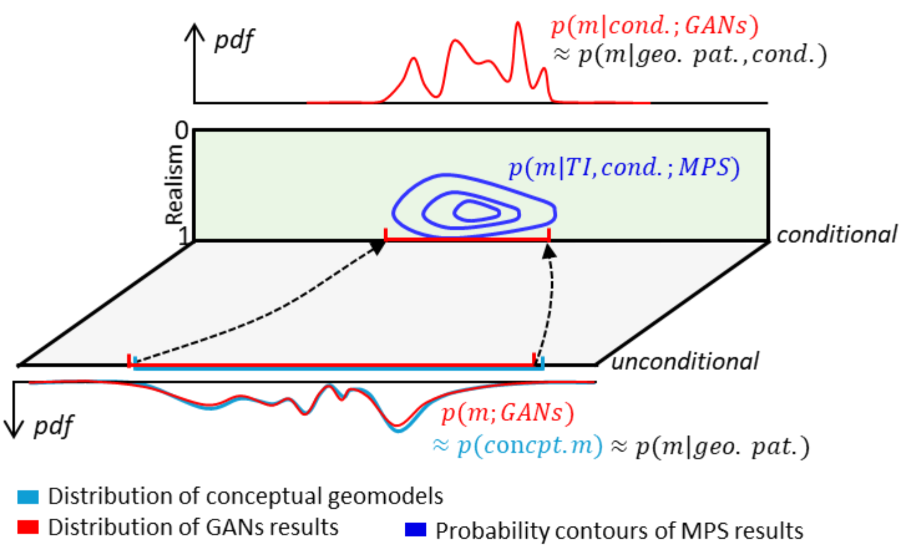

Figure 6. A schematic diagram showing the distributions of different types of geomodels.

3.2 Generation of nonstationary large geomodels

In GANSim, once trained, the Convolutional neural network (CNN)-based generator can be used to model reservoirs larger than the training conceptual geomodels. Additionally during inference, the input conditioning global feature maps (see Figure S1-1) are not necessarily constants as during the training time. Instead, spatially varying global feature maps can be taken into the trained generator. As shown in Figure 7 (a), in a large case of the fluvial channel scenario (with 128×128 cells), the input conditioning probability maps and the input channel direction map are specially designed so that a “divergent” shape of channels could be produced by the generator trained in Section 2.2. In the input global feature maps of the channel amplitude, wavelength, and width, the amplitude values are set to increase from the north to the south, while wavelength and width values are set to decrease along the same direction, thus a more sinuous and narrower channels are expected from the north to the south. In a large case of the point bar scenario (Figure 7 (b); with 192×192 cells), the input maps of the point bar-to-channel fill ratio and the floodplain proportion are also specially set so that the former feature gradually increase from the north to the south, while the latter decrease from the west to the east. Conditioning well facies are also given in the two cases. As shown in the generated realizations in Figure 7, all the expected nonstationary features are indeed produced in spite of some flaws in realism. For example, in the point bar case, the left channel belt keeps more floodplain than the right one, and from the north to the south the channel fill facies (green color) gradually narrows down to increase the point bar-to-channel fill ratio.

MPS can also produce some nonstationary features—e.g., the spatial change of geobody orientation and size—from stationary TIs by applying data events transformation filters (e.g., rotation, affinity and homothety) and probability aggregation schemes (e.g., the tau model proposed by Journel (2002)). See Mariethoz & Caers (2014) for detail. In comparison, GANSim produces geological features with the guidance of the global feature values and probability map values at each point. Once the global feature maps and probability maps exhibit certain level of non-stationarity, the corresponding nonstationary features would be generated in the resulting facies model.

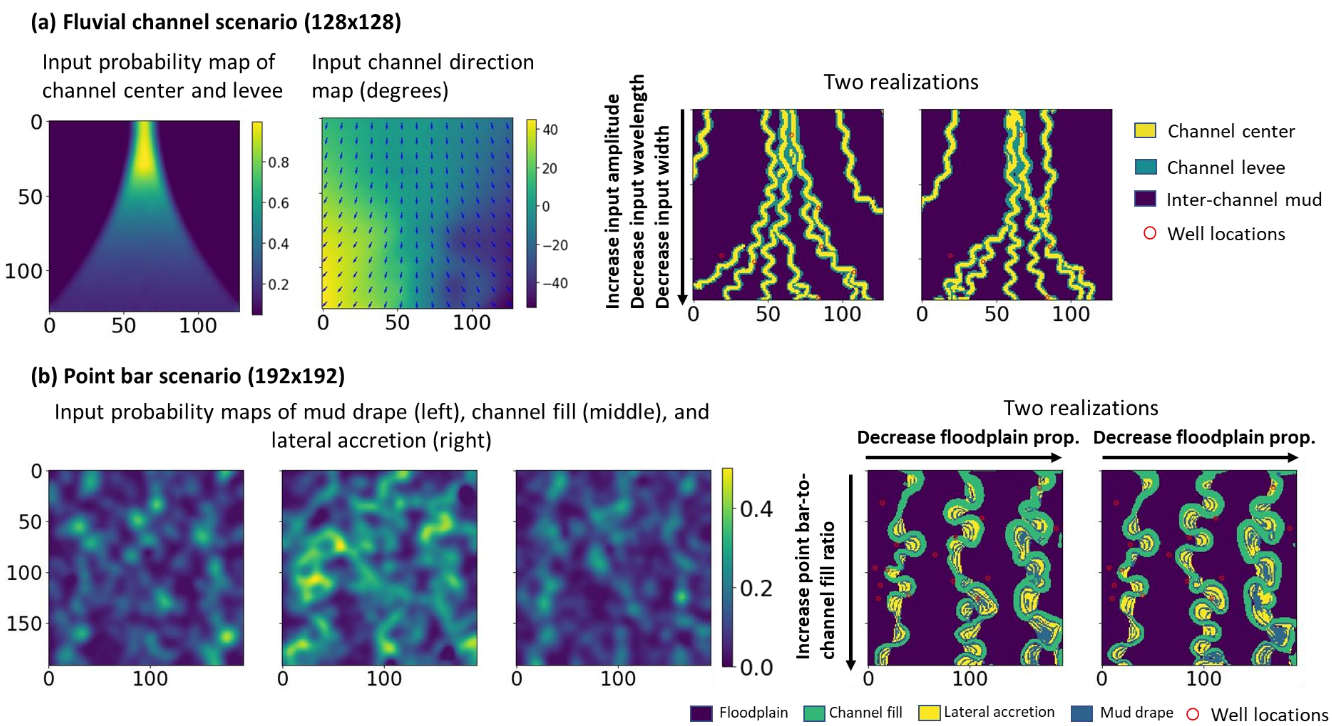

Figure 7. Geomodelling of nonstationary features using the pre-trained stationary generator for large reservoirs by taking in nonstationary global feature maps and probability maps.

4. Conclusions

This study presents a comparison between geostatistics-based and deep learning-based approaches for generative geomodelling using two distinct sedimentary reservoir scenarios: a fluvial channel system and a meandering point bar system. In particular, three typical MPS methods—Direct Sampling (DS), Quick Sampling (QS), and SNESIM—and two GAN-based workflows—post-GANs perturbation and GANSim with its latest enhancements—are examined in detail. Another enhancement for GANSim proposed in this paper is a redesigned input pipeline of global features in the generator. Instead of concatenating global features with latent vectors, the new design injects global features into various intermediate layers of the neural network.

The results clearly demonstrate that GAN-based workflows, particularly GANSim, consistently outperform MPS methods in generating geologically realistic facies model realizations, for the scenarios studied here. GANSim can directly condition on a wide range of data types, including global features, well facies data, and facies probability maps. In contrast, while MPS methods perform well in honoring well facies and probability map constraints—due to their algorithmic design—they produce facies models with significantly reduced geological realism. Conditioning on global features using MPS is also less reliable and highly dependent on the specific feature type. In terms of computational efficiency, the post-GANs workflow has a simulation speed comparable to that of MPS methods, whereas GANSim runs hundreds of times faster than MPS methods. Furthermore, the “single-pixel well facies overlook” issue identified in earlier versions of GANSim—which led to local disconnections near wells—has been effectively addressed by incorporating a local discriminator design, as proposed in Song et al. (2025). Flow simulation results indicate that the geomodels generated by GANSim produce more accurate and less uncertain predictions of flow behavior compared to those generated by SNESIM. This accuracy has important implications for subsequent decision-making in reservoir management. Finally, the flexibility of GANSim is demonstrated in its ability to generate large, nonstationary facies models using a generator trained only on stationary conceptual models. This is achieved by spatially varying the input global feature maps and carefully designing the conditioning probability maps. These capabilities position GANSim as a robust, scalable, and efficient solution for advanced generative geomodelling tasks.

One potential challenge of deep learning–based geomodelling approaches is the construction of numerous (many thousands) conceptual geomodels to train the generator. Efficient and automated process-mimicking or object-based modeling workflows may offer viable solutions. Recently, Wang et al. (2025) developed an image-warping workflow that integrates temporal remote sensing images of modern sedimentary evolution into conceptual geomodels, which may represent another promising direction for efficient conceptual geomodel construction.

Acknowledgments

We acknowledge the sponsors of the Stanford Center for Earth Resources Forecasting (SCERF). Some of the computing for this project was performed on the Sherlock cluster at Stanford University. We would like to thank Stanford University and the Stanford Research Computing Center for providing computational resources and support that contributed to these research results.

References

Alqassab, H. M., Feng, M., Becker, J. A., Song, S., & Mukerji, T. (2024). MAGCS: Machine Assisted Geologic Carbon Storage (Vol. ADIPEC, p. D021S044R001). https://doi.org/10.2118/222120-MS

Avseth, P., Mukerji, T., & Mavko, G. (2005). *Quantitative seismic interpretation: Applying rock physics tools to reduce interpretation risk*. Cambridge: Cambridge University Press. https://doi.org/10.1017/CBO9780511600074

Azevedo, L., & Soares, A. (2017). Geostatistical methods for reservoir geophysics. In *Advances in Oil and Gas Exploration and Production*.

Bortoli, L.-J., Alabert, F., Haas, A., & Journel, A. (1993). Constraining Stochastic Images to Seismic Data. https://doi.org/10.1007/978-94-011-1739-5_27

Bosch, M. (1999). Lithologic tomography: From plural geophysical data to lithology estimation. *Journal of Geophysical Research: Solid Earth*. https://doi.org/10.1029/1998jb900014

Bosch, M., Mukerji, T., & Gonzalez, E. F. (2010). Seismic inversion for reservoir properties combining statistical rock physics and geostatistics: A review. *Geophysics*. https://doi.org/10.1190/1.3478209

Buland, A., Kolbjørnsen, O., Hauge, R., Skjæveland, Ø., & Duffaut, K. (2008). Bayesian lithology and fluid prediction from seismic prestack data. *Geophysics*. https://doi.org/10.1190/1.2842150

Caers, J. (2003). History matching under training-image-based geological model constraints. *SPE Journal*, *8*(3), 218–226. https://doi.org/10.2118/74716-PA

Chan, S., & Elsheikh, A. H. (2019). Parametric generation of conditional geological realizations using generative neural networks. *Computational Geosciences*, *23*(5), 925–952. https://doi.org/10.1007/s10596-019-09850-7

Deutsch, C. V. (1992). *Annealing Techniques Applied to Reservoir Modeling and the Integration of Geological and Engineering (Well Test) Data*. Stanford University.

Doyen, P. (2007). *Seismic Reservoir Characterization: An Earth Modelling Perspective (EET 2)*. *Seismic Reservoir Characterization: An Earth Modelling Perspective (EET 2)*. https://doi.org/10.3997/9789073781771

Doyen, P. M. (1988). Porosity from seismic data: a geostatistical approach. *GEOPHYSICS*. https://doi.org/10.1190/1.1442404

Dupont, E., Zhang, T., Tilke, P., Liang, L., & Bailey, W. (2018). Generating realistic geology conditioned on physical measurements with Generative Adversarial Networks. In *Stat* (pp. 8–16).

Federico, G. Di, & Durlofsky, L. J. (2024). Latent diffusion models for parameterization and data assimilation of facies-based geomodels. Retrieved from https://arxiv.org/abs/2406.14815

De Figueiredo, L. P., Grana, D., Bordignon, F. L., Santos, M., Roisenberg, M., & Rodrigues, B. B. (2018). Joint Bayesian inversion based on rock-physics prior modeling for the estimation of spatially correlated reservoir properties. *Geophysics*. https://doi.org/10.1190/geo2017-0463.1

González, E. F., Mukerji, T., & Mavko, G. (2008). Seismic inversion combining rock physics and multiple-point geostatistics. *Geophysics*. https://doi.org/10.1190/1.2803748

Grana, D., Mukerji, T., & Doyen, P. (2021). *Seismic Reservoir Modeling*. *Seismic Reservoir Modeling*. https://doi.org/10.1002/9781119086215

Gravey, M., & Mariethoz, G. (2020). QuickSampling v1.0: A robust and simplified pixel-based multiple-point simulation approach. *Geoscientific Model Development*. https://doi.org/10.5194/gmd-13-2611-2020

Haas, A., & Dubrule, O. (1994). Geostatistical inversion - a sequential method of stochastic reservoir modelling constrained by seismic data. *First Break*. https://doi.org/10.3997/1365-2397.1994034

Hu, L. Y. (2000). Gradual deformation and iterative calibration of Gaussian-related stochastic models. *Mathematical Geology*. https://doi.org/10.1023/A:1007506918588

Hu, X., Song, S., Hou, J., Yin, Y., Hou, M., & Azevedo, L. (2024). Stochastic Modelling of Thin Mud Drapes inside Point Bar Reservoirs with ALLUVSIM-GANSim. *Water Resources Research*. https://doi.org/10.1029/2023WR035989

Journel, A. G. (2002). Combining knowledge from diverse sources: An alternative to traditional data independence hypotheses. *Mathematical Geology*, *34*(5), 573–596. https://doi.org/10.1023/A:1016047012594

Karssenberg, D., & Bridge, J. S. (2008). A three-dimensional numerical model of sediment transport, erosion and deposition within a network of channel belts, floodplain and hill slope: Extrinsic and intrinsic controls on floodplain dynamics and alluvial architecture. *Sedimentology*. https://doi.org/10.1111/j.1365-3091.2008.00965.x

Laloy, E., Hérault, R., Lee, J., Jacques, D., & Linde, N. (2017). Inversion using a new low-dimensional representation of complex binary geological media based on a deep neural network. *Advances in Water Resources*, *110*, 387–405. https://doi.org/10.1016/j.advwatres.2017.09.029

Laloy, E., Hérault, R., Jacques, D., & Linde, N. (2018). Training-image based geostatistical inversion using a spatial Generative Adversarial Neural Network. *Water Resources Research*, *54*(1), 381–406. https://doi.org/10.1002/2017WR022148

Lee, D., Ovanger, O., Eidsvik, J., Aune, E., Skauvold, J., & Hauge, R. (2023). Latent Diffusion Model for Conditional Reservoir Facies Generation. *arXiv Preprint arXiv:2311.01968*.

Lee, D., Ovanger, O., Eidsvik, J., Aune, E., Skauvold, J., & Hauge, R. (2025). Latent diffusion model for conditional reservoir facies generation. *Computers & Geosciences*, *194*, 105750. https://doi.org/https://doi.org/10.1016/j.cageo.2024.105750

Mariethoz, G., & Caers, J. (2014). *Multiple-point geostatistics: stochastic modeling with training images*. New York: John Wiley & Sons. https://doi.org/10.1002/9781118662953

Mariethoz, G., Renard, P., & Straubhaar, J. (2010). The direct sampling method to perform multiple-point geostatistical simulations. *Water Resources Research*, *46*(11), 1–14. https://doi.org/10.1029/2008WR007621

McHargue, T., Pyrcz, M. J., Sullivan, M. D., Clark, J. D., Fildani, A., Romans, B. W., et al. (2011). Architecture of turbidite channel systems on the continental slope: Patterns and predictions. *Marine and Petroleum Geology*. https://doi.org/10.1016/j.marpetgeo.2010.07.008

Mo, S., Zabaras, N., Shi, X., & Wu, J. (2020). Integration of Adversarial Autoencoders With Residual Dense Convolutional Networks for Estimation of Non-Gaussian Hydraulic Conductivities. *Water Resources Research*. https://doi.org/10.1029/2019WR026082

Mosser, L., Dubrule, O., & Blunt, M. J. (2020). Stochastic seismic waveform inversion using Generative

Adversarial Networks as a geological prior. *Mathematical Geosciences*, *52*(1), 53–79. https://doi.org/10.1007/s11004-019-09832-6

Nesvold, E., & Mukerji, T. (2021). Simulation of fluvial patterns with GANs trained on a data set of satellite imagery. *Water Resources Research*, *57*(22). https://doi.org/10.1029/2019WR025787.

Pyrcz, M. J., & Deutsch, C. V. (2014). *Geostatistical Reservoir Modeling* (2nd ed.). Oxford University Press.

Pyrcz, M. J., Boisvert, J. B., & Deutsch, C. V. (2009). ALLUVSIM: A program for event-based stochastic modeling of fluvial depositional systems. *Computers and Geosciences*. https://doi.org/10.1016/j.cageo.2008.09.012

Song, S., Mukerji, T., & Hou, J. (2021a). GANSim: Conditional Facies Simulation Using an Improved Progressive Growing of Generative Adversarial Networks (GANs). *Mathematical Geosciences*. https://doi.org/10.1007/s11004-021-09934-0

Song, S., Mukerji, T., & Hou, J. (2021b). Geological Facies modeling based on progressive growing of generative adversarial networks (GANs). *Computational Geosciences*. https://doi.org/10.1007/s10596-021-10059-w

Song, S., Mukerji, T., & Hou, J. (2022a). Bridging the Gap between Geophysics and Geology with Generative Adversarial Networks. *IEEE Transactions on Geoscience and Remote Sensing*. https://doi.org/10.1109/TGRS.2021.3066975

Song, S., Mukerji, T., Hou, J., Zhang, D., & Lyu, X. (2022b). GANSim-3D for conditional geomodelling: theory and field application. *Water Resources Research, 58*. https://doi.org/doi.org/10.1029/2021WR031865

Song, S., Zhang, D., Mukerji, T., & Wang, N. (2023). GANSim-surrogate: An integrated framework for stochastic conditional geomodelling. *Journal of Hydrology*. https://doi.org/10.1016/j.jhydrol.2023.129493

Song, S., Mukerji, T., & Zhang, D. (2025). Physics-informed multi-grid neural operator: Theory and an application to porous flow simulation. *Journal of Computational Physics*, *520*, 113438. https://doi.org/https://doi.org/10.1016/j.jcp.2024.113438

Song, S., Mukerji, T., Scheidt, C., Alqassab, H., & Feng, M., Geomodelling of multi-scenario non-stationary reservoirs with enhanced GANSim. Under review. 2025.

Strebelle, S. (2002). Conditional simulation of complex geological structures using multiple-point statistics. *Mathematical Geology*, *34*(1), 1–21. https://doi.org/10.1023/A:1014009426274

Sun, T., Ghayour, K., Hall, B., & Miller, J. (2010). Process-Based Modeling of Deep Water Depositional Systems. In *Seismic Imaging of Depositional and Geomorphic Systems: 30th Annual*. https://doi.org/10.5724/gcs.10.30.0088

Sylvester, Z., Pirmez, C., & Cantelli, A. (2011). A model of submarine channel-levee evolution based on channel trajectories: Implications for stratigraphic architecture. *Marine and Petroleum Geology*, *28*(3), 716–727. https://doi.org/10.1016/j.marpetgeo.2010.05.012

Wang, Y., Storms, J. E. A., Martinius, A. W., Karssenberg, D., & Abels, H. A. (2021). Evaluating alluvial stratigraphic response to cyclic and non-cyclic upstream forcing through process-based alluvial architecture modelling. *Basin Research*. https://doi.org/10.1111/bre.12454

Wang, Y., Li, Y., & Limaye, A. B. (2025). Bridging gaps in satellite observations of river and delta landscapes using image warping. *Water Resources Research*, *61*(5), e2024WR039854.

Xu, M., Song, S., & Mukerji, T. (2024). DiffSim: Denoising diffusion probabilistic models for generative facies geomodeling. In *Fourth International Meeting for Applied Geoscience & Energy* (pp. 1660–1664). https://doi.org/10.1190/image2024-4081304.1

Yan, N., Mountney, N. P., Colombera, L., & Dorrell, R. M. (2017). A 3D forward stratigraphic model of fluvial meander-bend evolution for prediction of point-bar lithofacies architecture. *Computers and Geosciences*. https://doi.org/10.1016/j.cageo.2017.04.012

Zhang, T. F., Tilke, P., Dupont, E., Zhu, L. C., Liang, L., & Bailey, W. (2019). Generating geologically realistic 3D reservoir facies models using deep learning of sedimentary architecture with generative adversarial networks. *Petroleum Science*, *16*(3), 541–549. https://doi.org/10.1007/s12182-019-0328-4

Supporting Information for

Generative geomodelling: Deep Learning vs. Geostatistics

Suihong Song[1,*], Jiayuan Huang[1], Tapan Mukerji[1]

[1] Stanford University, 367 Panama St, Stanford, CA 94305, USA

Corresponding author: Suihong Song (suihong@stanford.edu)

Supporting Information S1

Latest GANSim Enhancements and the neural network architectures used in this paper

Earlier versions of GANSim faced a challenge where well facies data represented by single horizontal pixels were often overlooked by the discriminator. This led to noticeable local disconnections between the conditioning well facies data and the surrounding regions of the same facies type. To alleviate this issue, the well facies data were artificially expanded from single pixels to larger patches horizontally (e.g., 4×4 pixels), as suggested by Song et al. (2021b, 2022). While this approach helped reduce disconnections, it introduced local artifacts and artificially constrained the uncertainty near wells. To overcome these limitations, Song et al. (2025) introduced local discriminators specially scrutinizing local realisms around well facies data in addition to the "global" discriminator focusing more on the global realism of the domain. Multiple local discriminators can be designed to focus on different sizes of locality around wells. These local discriminators can be separate from or integrated into the global discriminator where different discriminators share the same shallow convolutional layers in the integration design. Both separate and integrated architectures prove to produce similar results. Note the Wasserstein loss function with gradient penalty (Gulrajani et al., 2017) is used in GANSim. Experiments show that the generator can produce good local and global realism by summing up the Wasserstein losses of different discriminators instead of summing up the scores of different discriminators first and then calculating a Wasserstein loss for the score resulting from summation. Weights should be set for the Wasserstein losses of different discriminators when summing up. With local discriminator design, the well facies data expansion approach is not necessary, which alleviates the artifact problem of expanded well facies data.

Another improvement proposed by Song et al. (2025) involves modifying the generator output and discriminator input from a single facies geomodel to multiple facies indicators (i.e., one-hot encoding) each corresponding to one facies type (see Figure S1-1). In inference, these facies indicators produced by the trained generator can be converted into a reservoir facies model through argmax or thresholding-related operations. Such a design of multiple facies indicators is more reasonable and common in variogram-based geomodelling algorithms such as sequential indicator simulation (Pyrcz & Deutsch, 2014). Based on the above enhancements, GANSim has already been successfully applied in a field 3D deltaic reservoir (Alqassab et al., 2024).

Regarding the input pipeline of conditioning global features, the previous design of concatenating global feature values to the input latent cube proved efficient when considering mud proportion, channel width, and channel sinuosity in Song et al. (2021b), but it is challenging when channel direction is taken as the input global feature. After experiments, we found that a similar design of the global feature input pipeline to that of well facies and probability maps is much more efficient than the previous design, which is possibly due to the flexible information transmission mechanism from shallow to deep layers.

For better understanding of the above enhancements either proposed by both Song et al. (2025) and this paper, the GANSim architecture used for geomodelling of fluvial channel scenario of this paper is presented here in Figure S1-1. Five types of global features are considered in this case: channel direction, mud facies proportion, channel width, channel wavelength, and channel amplitude. Channel direction is equally discretized into 30 categories. In the generator, the input global features are expanded into 34 maps (i.e., 64x64x34) with the first 30 maps expanded from the one-hot vector of the channel direction category and the remaining 4 maps corresponding to the other 4 global feature types. A global feature value is replicated across the entire map. The feature cube is then downsampled into different sizes and concatenated into different feature cubes of the main pipeline of the generator. The generator use fully convolutional layer design to allow for geomodelling of arbitrarily large reservoir domains after training, which was proposed by Song et al. (2022). Three facies types are considered, so the output of the generator and the input of the discriminator include three channels of facies indicators, i.e., 64x64x3. The final activation function before the output facies indicators of the generator is set as a softmax function. There is one global and three local discriminators combined. In each local discriminator, following several convolutional and downsampling layers that are shared by the global discriminator and three separate convolutional layers with the kernel size of 1x1, a small-size feature map is finally produced wherein each feature value of a cell is expected to represent the realism of a local area of the input reservoir domain. Then, through an element-wise multiplication between the small-size feature map and a downsampled well location indicator map (having the same size as the feature map) and an averaging calculation, a 1x1-size local score is produced which represents the local realism around all well facies data for a specific locality level. The output score value of the local discriminator 1 reveals the average realism of a locality of 4x4 cells around all wells, while that of the local discriminator 2 and 3 correspond to the realism of a locality of 12x12 and 28x28 cells around all wells. The GANSim architectures used for the point bar scenario is similar to Figure S1-1, except the input global feature types and numbers and the facies types.

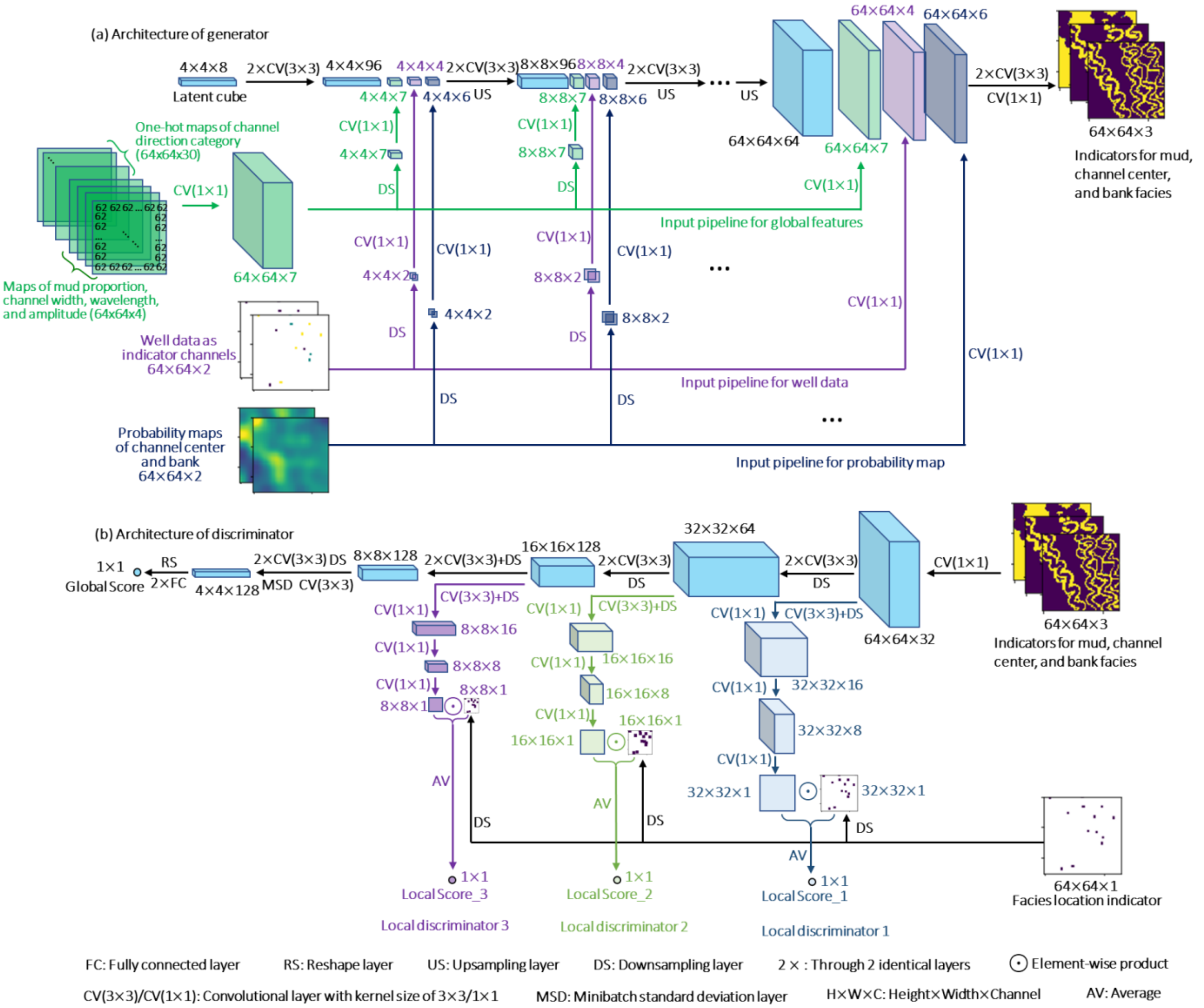

Figure S1-1. The generator and discriminator architectures used for geomodelling of channel scenario in this paper.

Supporting Information S2

Materials related to fluvial channel scenario in Section 2.1

1. Training and evaluation of unconditional GANs

The convolutional neural network architectures of the generator and the discriminator are shown in Figure S1-1 of Supporting Information S1, where the input pipelines of different conditions in the generator and the local discriminator branches of the discriminator are excluded. The minibatch size is set as 128. Learning rate is set as 0.0025. Adam optimizer (Kingma & Ba, 2014) with the default parameters are used during training. The generator is trained on 1 GPUs (A100) for 6 hours when the generated facies models are realistic by visual inspection. After training, evaluations based on visual inspection, multi-scale sliced Wasserstein distance and multi-dimensional scaling plots (MDS), facies proportion, and global feature probability density functions are performed (Figure S2-1). The global feature values of generated facies models are captured based on a global feature recognizer neural network (see part 3 of this Supporting Information). Song et al. (2021a) gives more detail about the multi-scale sliced Wasserstein distance combined with multi-dimensional scaling plot method. It turns out that the trained generator can produce diverse and realistic facies models compared to test ones.

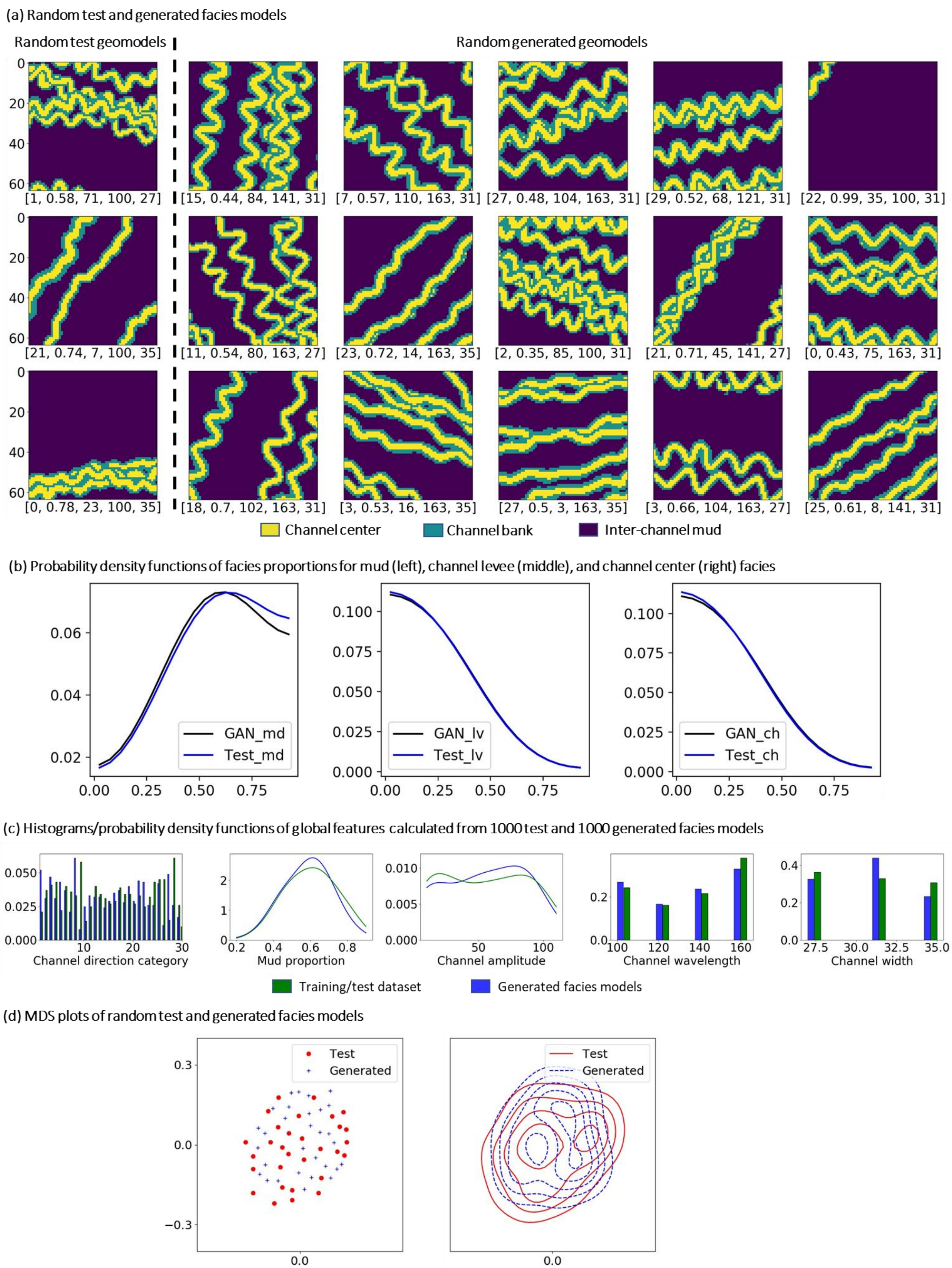

(a) Random test and generated facies models
Random test geomodels
Random generated geomodels
[1, 0.58, 71, 100, 27]
[15, 0.44, 84, 141, 31]
[7, 0.57, 110, 163, 31]
[27, 0.48, 104, 163, 31]
[29, 0.52, 68, 121, 31]
[22, 0.99, 35, 100, 31]
[21, 0.74, 7, 100, 35]
[11, 0.54, 80, 163, 27]
[23, 0.72, 14, 163, 35]
[2, 0.35, 85, 100, 31]
[21, 0.71, 45, 141, 27]
[0, 0.43, 75, 163, 31]
[0, 0.78, 23, 100, 35]
[18, 0.7, 102, 163, 31]
[3, 0.53, 16, 163, 35]
[27, 0.5, 3, 163, 35]
[3, 0.66, 104, 163, 27]
[25, 0.61, 8, 141, 31]
Channel center
Channel bank
Inter-channel mud
(b) Probability density functions of facies proportions for mud (left), channel levee (middle), and channel center (right) facies
GAN_md
Test_md
GAN_lv
Test_lv
GAN_ch
Test_ch
(c) Histograms/probability density functions of global features calculated from 1000 test and 1000 generated facies models
Channel direction category
Mud proportion
Channel amplitude
Channel wavelength
Channel width
Training/test dataset
Generated facies models
(d) MDS plots of random test and generated facies models
Test
Generated

Figure S2-1. Comparison between generated and test facies models in visual inspection, facies proportions, global feature distributions, and MDS plots. The values inside the brackets below facies models are channel direction category, mud proportion, channel amplitude, channel wavelength, and channel width. Global features in sub-figure (a) and (c) are calculated with the global feature recognizer neural network.

2. Training and evaluation of the global feature recognizer neural network

The architecture of the recognizer neural network is adapted from the unconditional discriminator in Figure S1-1: the local discriminator branches are excluded, the output of the discriminator is changed from having only 1 neuron into containing 34 neurons, among which the first 30 neurons—forming a one-hot vector—correspond to the 30 channel direction categories, and the remaining 4 neurons correspond to mud proportion, channel center width, channel wavelength, and channel amplitude. The loss functions include a categorical cross-entropy loss for the channel direction categorical feature and L2 losses for the remaining features. During training, no progressive growing is performed. The recognizer is trained with the training conceptual geomodel-global feature data pairs using 3 hours on one GPU(A100).

To evaluate the trained recognizer, we take 3000 test facies models into the trained recognizer and compare the output global feature values with their global feature labels. The results are shown in Figure S2-2. It is clear that the recognizer is very accurate in identifying the mud proportion. However, for the other 4 global features, the recognizer is not very accurate. The major reason is that when constructing the dataset, the mud proportion label is calculated from the conceptual facies model, while the other global feature labels are actually the input parameters into the object-based algorithm for generating conceptual facies models (see Song et al. (2021a) for detail). By design, the object-based algorithm adds a drift of 20% - 30% to these input global parameters (labels), thus making the real global features fluctuate around the labels, to some extent, or even mix into surrounding labels. The blue dashed curves in Figure S2-2 outline the range of real global features, and the recognized global feature values just fall inside these real feature ranges. This indicates the trained recognizer can accurately capture the real global feature values, in spite of noises in the training global feature labels.

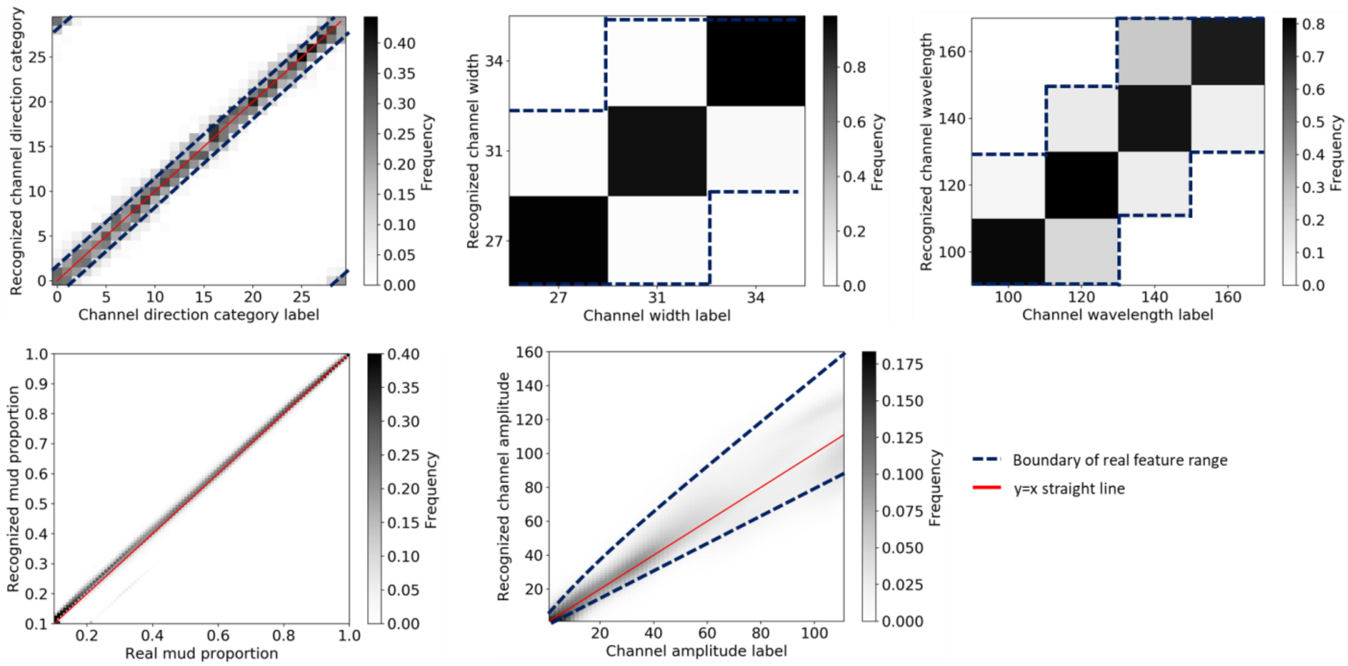

Figure S2-2. Comparison between global feature labels and the recognized global features calculated by the trained recognizer neural network, based on 3,000 test facies models. The grey color of each pixel represents the frequency of the corresponding y-axis value (recognized feature) given the x-axis value (feature label), i.e., $p(y|x)$. The blue dash curves outline the real global feature ranges.

3. Enhanced architecture of GANSim and hyperparameter settings

The architectures of the generator and discriminator are adapted from Figure S1-1. The input pipelines for the well facies data and the probability maps are excluded in the generator. In the discriminator, the local discriminator branches are also excluded. We initially tried the previous design of global feature input pipeline of GANSim that the global features are concatenated with the input latent cube (Song et al., 2021b), but the conditioning effects are not apparent when the channel direction global feature is considered. After experiments, we propose to inject input global features into different middle neural layers of the generator, the similar input manner as the input well facies and input probability maps. See Supporting Information S1 for more detail.

There are totally 6 loss terms: the original GANs loss and five condition-based losses of the five global features. After trial-and-error experiments, the weights are set as in Table S2-1. Other hyperparameters are the same as for the training of the unconditional GANs in Section 1 of this Supporting Information.

Table S2-1. Weights for different loss terms in GANSim conditioned only to global features in fluvial scenario

Original GANs loss	Channel direction loss	Mud proportion loss	Channel width loss	Channel wavelength loss	Channel amplitude loss
3	15	1.2	1	1.5	2

4. Simulation results of different MPS parameters

Different hyperparameters have been explored for the three MPS approaches—direct sampling (Mariethoz et al., 2010), quick sampling (Gravey & Mariethoz, 2020), and SNESIM method (Strebelle, 2002) of Petrel software (the "Multipoint simulation with pattern objects" algorithm in Petrel). In direct sampling method (DS), the maximum fraction of TI to scan (f) is fixed at 100% to guarantee the best performance in the results, while the closest neighbors to consider (n) and the similarity distance threshold (t) are independently sampled from [5, 10, 15, 20] and [0.01, 0.1]. Some random simulated facies model realizations are shown in Figure S2-3 (b). We found that when n is larger than 20, although the produced realism and connectivity becomes better but there is a trend that the simulation process copies a complete portion from the TI, e.g., compare the realization and the TI portion both marked by red rectangles in Figure S2-3 (a) and (b) where the repetition rate is 89%. Such a "copy" artifact would largely reduce the diversity of the produced realizations. When t is smaller than 0.01, it has no effect on the results, and when t is larger than 0.1, the simulation results gradually become very noisy. Based on these analyses, we select the realizations from the parameter combination of (n = 15, t = 0.1), which do not have a very high repetition rate to TI but exhibit relatively good realism, as the final results (see Figure 1).

Important parameters in quick sampling (QS) approach include the closest neighbors to consider (n) and the number of best pattern candidates (k) from TI. Here, n and k are independently sampled from [5, 10, 15, 20] and [1, 3]. Random realizations of these parameter combinations are shown in Figure S2-3 (c). Similar to direct sampling approach, larger n lead to more likely a copy from the TI, e.g., the realization and the TI portion marked by blue rectangles look quite similar with a repetition rate of 81%. The parameter k has almost no effect on the simulation results when k is smaller than 5, and when it is larger than 5, many small noises gradually appear weakening the produced realism. In this paper, the parameter combination of (n = 15, k = 1) is used to simulate the final results (Figure 1).

In SNESIM approach, the search radius for conditioning neighbors (r) is the most important parameters influencing the simulation performances, which may relate to the parameter n in DS and QS, to some extent. We explored radius from 2 to 8, and found the larger the parameter r is the more apparent the copy artifacts become, e.g., the realization and the TI portion marked by green rectangles are almost the same with a repetition rate of 99%. We finally choose r = 5 to simulate the final results (Figure 1). It should be noted that produced facies models corresponding to the selected parameters of the three MPS approaches are comparable, because they exhibit close repetition rate—i.e., 72%, 71%, and 70% in DS, QS, and SNESIM.

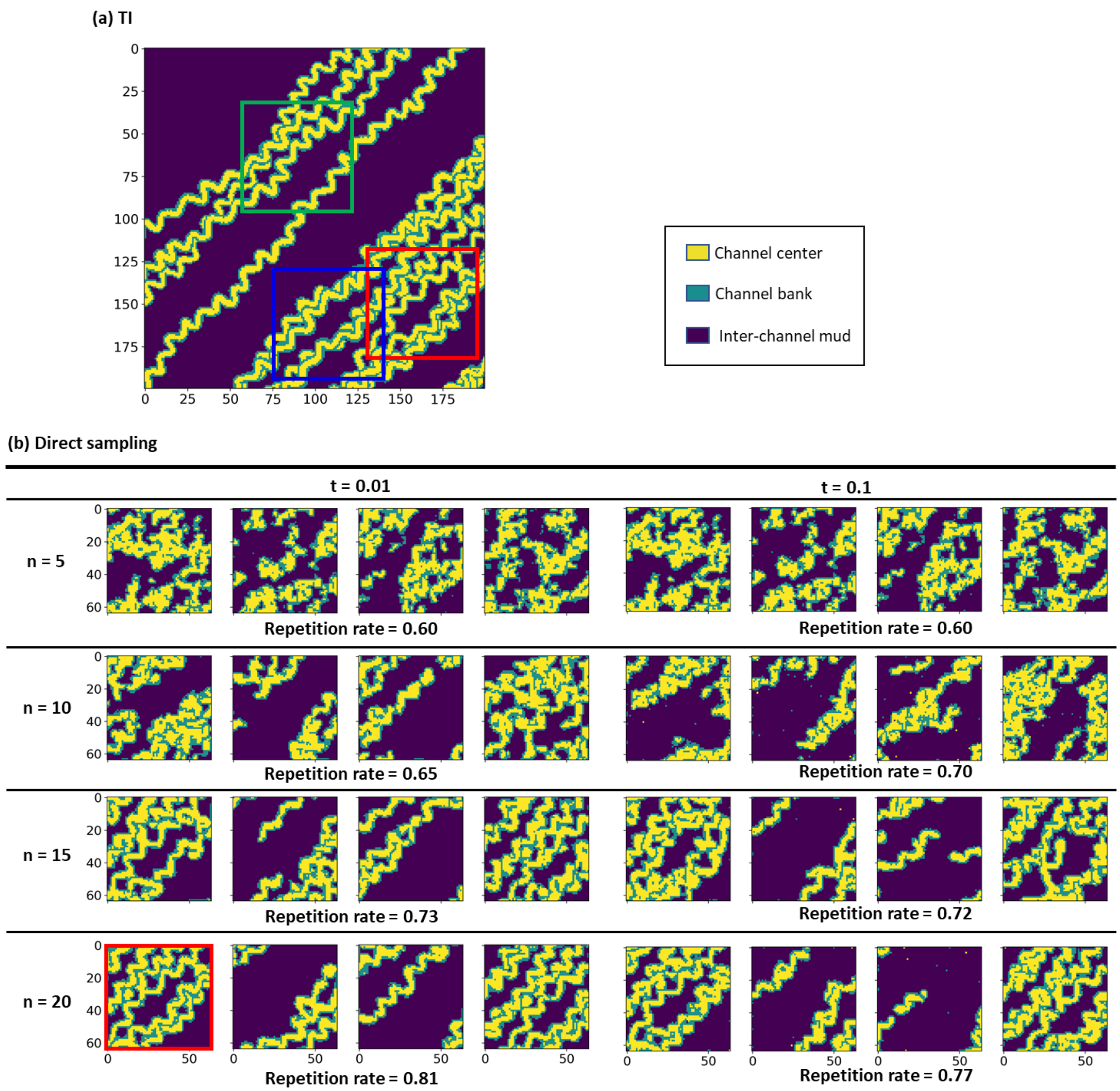
(a) TI
Channel center
Channel bank
Inter-channel mud
(b) Direct sampling
t = 0.01
t = 0.1
n = 5
Repetition rate = 0.60
Repetition rate = 0.60
n = 10
Repetition rate = 0.65
Repetition rate = 0.70
n = 15
Repetition rate = 0.73
Repetition rate = 0.72
n = 20
Repetition rate = 0.81
Repetition rate = 0.77

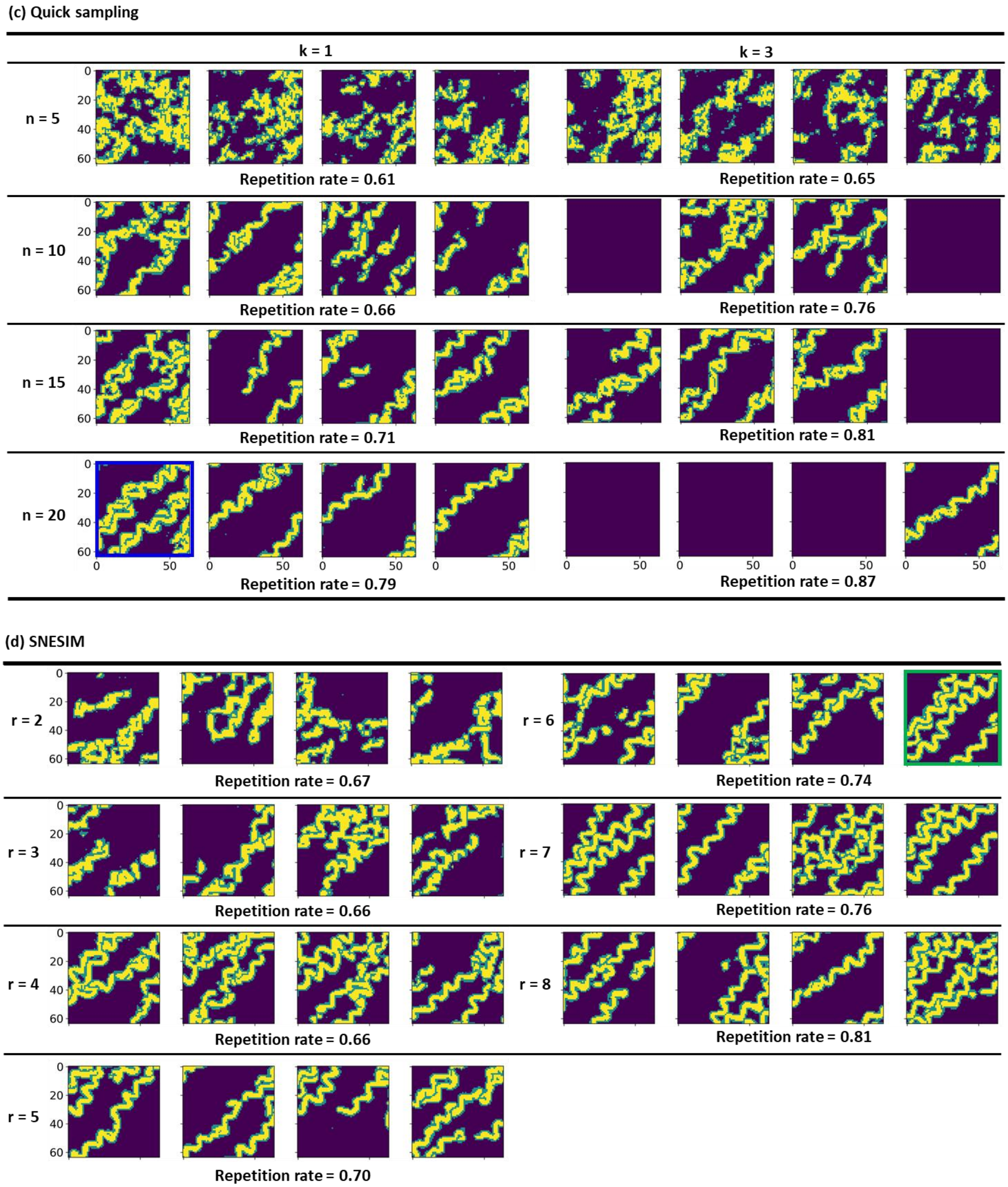

Figure S2-3. The applied training image (TI) and simulation results of direct sampling (DS), quick sampling (QS), and SNESIM with different parameter combinations. The “repetition rate” is averaged from 100 realizations.

Supporting Information S3

Materials related to point bar scenario in Section 2.1

1. Training and evaluation of unconditional GANs

The architectures of the generator and the discriminator are almost the same as in the previous fluvial channel scenario, except for the output of the generator and the input of the discriminator which is adapted from 3 facies indicators into 4 indicators corresponding to the 4 facies types of this scenario. Other hyperparameters are the same as the channel scenario. The generator is trained on 1 GPUs (A100) for 6 hours when the generated facies models are realistic by visual inspection. Evaluations based on visual inspection, multi-scale sliced Wasserstein distance and multi-dimensional scaling plots (MDS), facies proportion, and global feature probability density functions are performed (Figure S3-1). It turns out that the trained generator can produce diverse and realistic facies models compared to test ones.

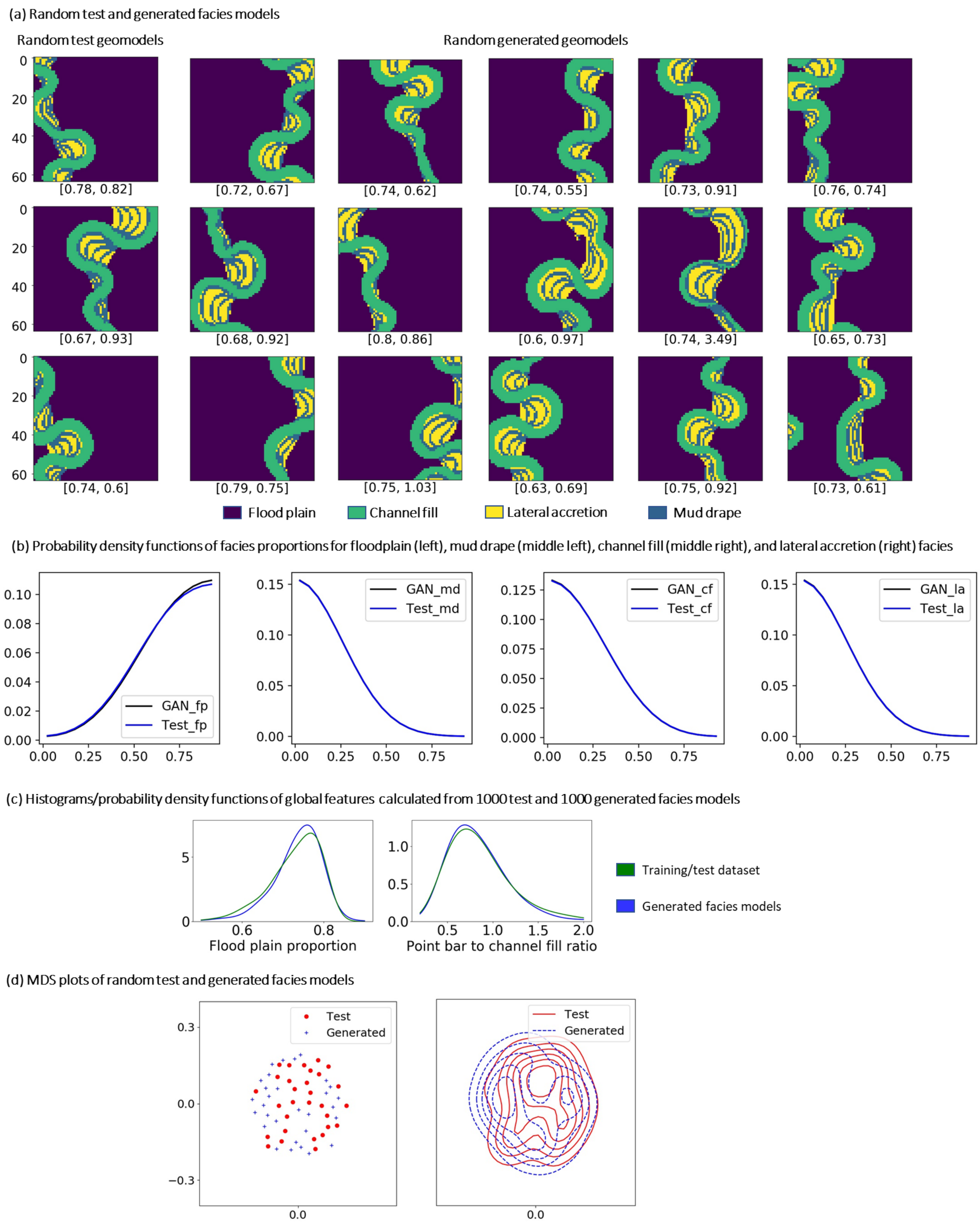

(a) Random test and generated facies models
Random test geomodels
Random generated geomodels
[0.78, 0.82]
[0.72, 0.67]
[0.74, 0.62]
[0.74, 0.55]
[0.73, 0.91]
[0.76, 0.74]
[0.67, 0.93]
[0.68, 0.92]
[0.8, 0.86]
[0.6, 0.97]
[0.74, 3.49]
[0.65, 0.73]
[0.74, 0.6]
[0.79, 0.75]
[0.75, 1.03]
[0.63, 0.69]
[0.75, 0.92]
[0.73, 0.61]
Flood plain
Channel fill
Lateral accretion
Mud drape
(b) Probability density functions of facies proportions for floodplain (left), mud drape (middle left), channel fill (middle right), and lateral accretion (right) facies
GAN_fp
Test_fp
GAN_md
Test_md
GAN_cf
Test_cf
GAN_la
Test_la
(c) Histograms/probability density functions of global features calculated from 1000 test and 1000 generated facies models
Flood plain proportion
Point bar to channel fill ratio
Training/test dataset
Generated facies models
(d) MDS plots of random test and generated facies models
Test
Generated

Figure S3-1. Comparison between generated and test facies models in visual inspection, facies proportions, global feature distributions, and MDS plots. The values inside the brackets below facies models are floodplain proportion and point bar-to-channel fill ratio.

2. Hyperparameters and architecture of GANSim

The architectures of the generator and discriminator are almost the same as the fluvial scenario except the number of facies indicator maps (in the output of the generator and input of the discriminator) and the number of input global features. L2 loss functions are used for the two global features. The weights for the original GANs loss and the condition-based losses for the two global features are set as in Table S3-1, after trial-and-error experiments. Other hyperparameters are the same as in the fluvial scenario.

Table S3-1. Weights of different loss terms in GANSim conditioned only to global features in point bar scenario

Original GANs loss	Floodplain proportion loss	Point bar-to-channel fill ratio loss
8	1	1.5

3. Simulation results of different MPS parameters

We explored the parameter combinations for the three MPS approaches with the same processes as in the fluvial channel scenario and obtained almost the same conclusions. The simulation results with different parameters of the three approaches are shown in Figure S3-2. Note that in this figure, the simulation results of parameter k = 5 are shown instead of k = 3 in the fluvial channel scenario, since most realizations of k = 3 here are pure floodplain facies. Finally, the parameter combination of (n = 15, t = 0.1) in DS, (n = 15, k = 1) in QS, and r = 5 in SNESIM are regarded as the best, because their simulation results exhibit a certain level of expected realism yet not replicate too much from TI. Also, the produced facies models corresponding to these selected parameters of the three MPS approaches are comparable, because they exhibit close repetition rate—i.e., 80%, 78%, and 77% in DS, QS, and SNESIM. These resulted facies model realizations are compared with GANs results in Figure 2.

(a) TI

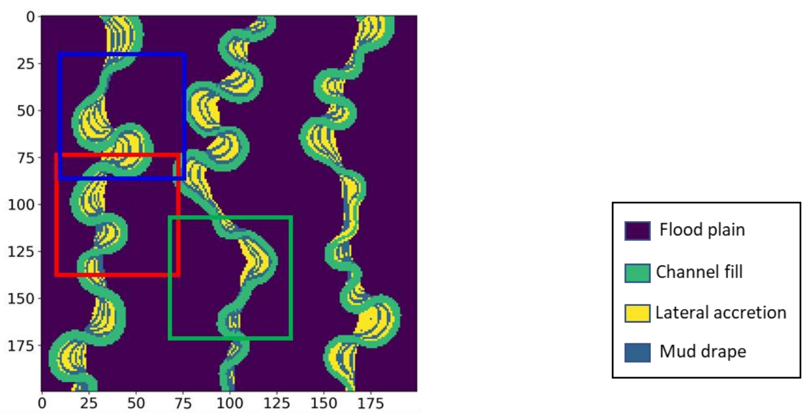

(b) Direct sampling

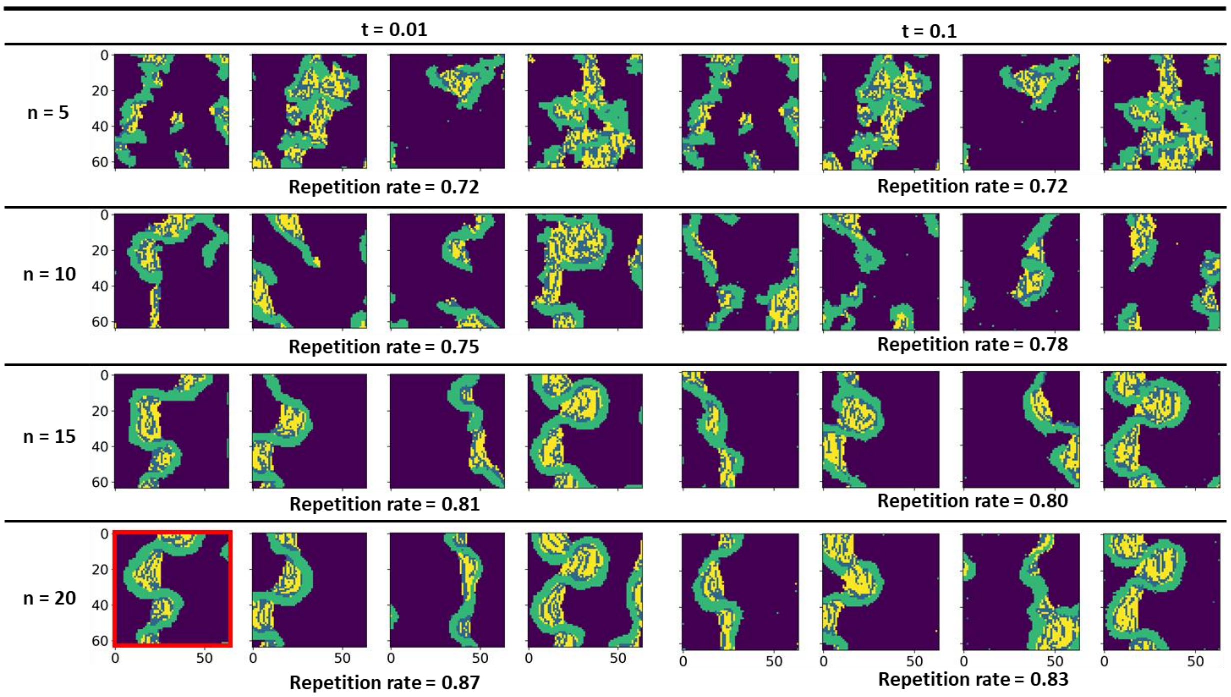

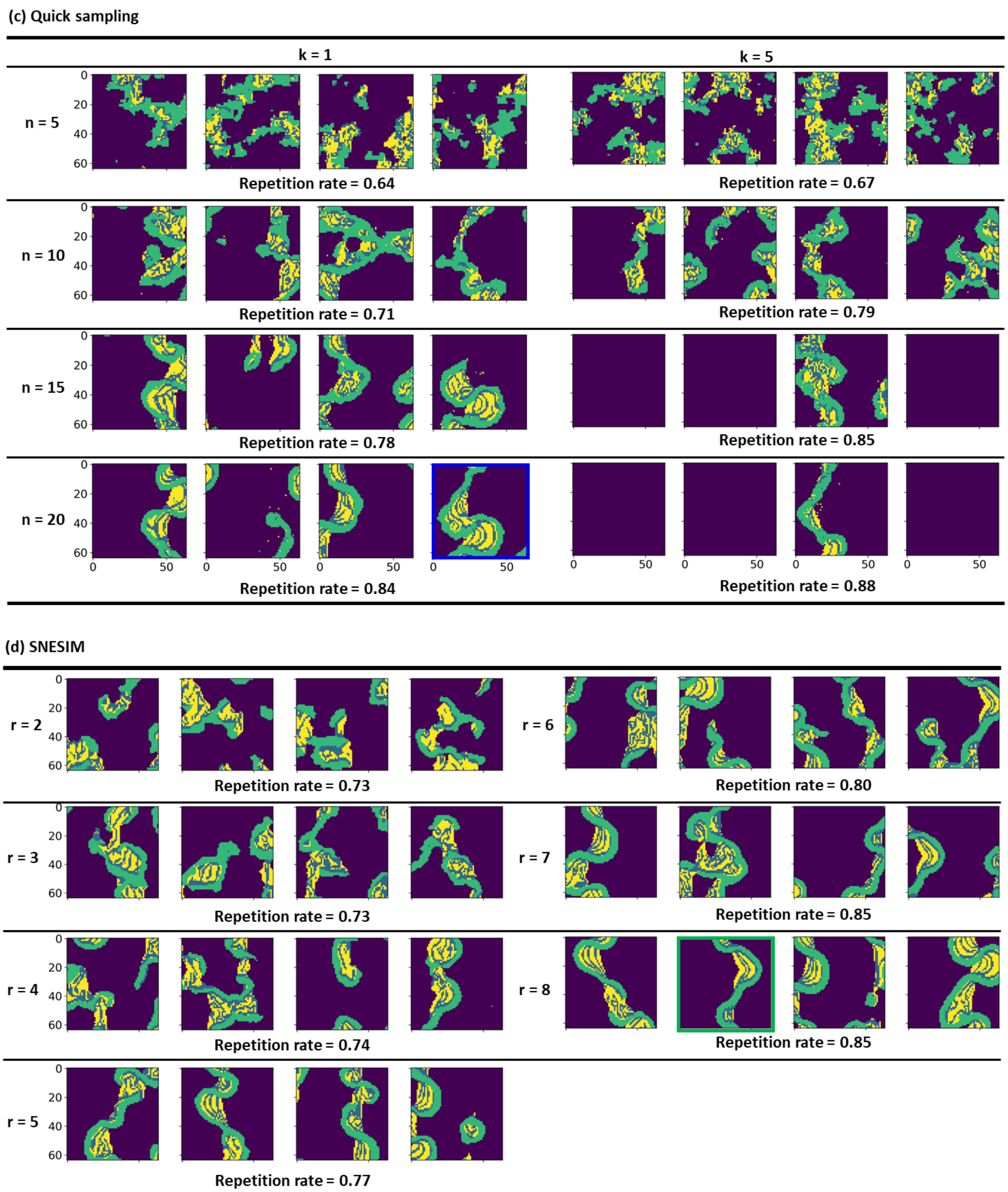

Figure S3-2. The applied training image (TI) and simulation results of direct sampling (DS), quick sampling (QS), and SNESIM with different parameter combinations. The “repetition rate” is averaged from 100 realizations.

Supporting Information S4

Materials related to Section 2.2

1. GANSim training for both scenarios

The architectures of the generator and the discriminator of the fluvial channel scenario are illustrated in Figure S1-1. The input pipeline for global features are almost the same as for well facies and probability maps. Three local discriminators are designed with the local scrutinization domain of 4x4, 12x12, and 28x28 cells from small to large local discriminators. The weights for small, middle, and large local discriminator losses are 0.2, 1, and 5, respectively. The weights of different loss terms are set as in Table S4-1, after many trial-and-error experiments. Other hyperparameters are the same as in GANSim only conditioning to global features. The training takes 10 hours in parallel on 2 GPUs (A100). We also tried the previous design of global feature input pipeline of GANSim that the global features are concatenated with the input latent cube, but the conditioning effects are not apparent when the channel direction global feature is considered due to unknown reasons. It should be noted that the current input method of different conditioning data is very similar to that in style GANs (Karras et al., 2018) where noises and conditions are all introduced into the backbone of the generator at different depth of the architecture. We should also be careful that when only considering conditioning of well facies and probability maps, the scrutinization domains of local discriminators could be relatively larger, e.g., the scrutinization domain of the small local discriminator can be 6x6-cell areas around wells, but with additional global features as conditions, the scrutinization domains have to be set smaller, e.g., 4x4-cell areas around wells.

Table S4-1. Weights for different loss terms in GANSim conditioned to global features, well facies, and probability maps in fluvial scenario

Original GANs loss	Discriminator loss				Well facies loss
	Global discriminator	Small local discriminator	Middle local discriminator	Large local discriminator	
40	0.2	0.16	0.8	4	1500
Probability map loss	Channel direction loss	Mud proportion loss	Channel width loss	Channel wavelength loss	Channel amplitude loss
2	35	0.03	0.4	1.2	5

The GANSim architectures of the point bar scenario are almost the same as in the fluvial scenario, with the only difference being the number of global features and facies indicator maps (in the output of the generator and input of the discriminator). The weights of different loss terms are shown in Table S4-2 after trial-and-error experiments. Other hyperparameters are the same as in GANSim only conditioning to global features. It is trained at 2 GPUs (A100) for 9 hours.

Table S4-2. Weights for different loss terms in GANSim conditioned to global features, well facies, and probability maps in point bar scenario

Discriminator loss

Original GANs loss	Global discriminator	Small local discriminator	Middle local discriminator	Large local discriminator
60	0.08	4.6	0.92	0.184
Well facies loss	Probability map loss	Floodplain proportion loss	Point bar-to-channel fill loss	
100	2	2	1.5	

2. SNESIM simulation

Only SNESIM is used for geomodelling when conditioning to all the three types of data among the three MPS approaches. Based on the investigations of the previous cases only conditioning to global features, the search radius for conditioning neighbors (r) is set as 5. The multi-grids technique of 3 levels is applied. The "trust fraction" to honor the facies proportion of TIs is set as 0.5. The tau model is used by default to integrate the probability values obtained from the TI and the conditioning facies probability maps, with the weights of the probability values of both sources set as 1. The simulation of each realization takes 0.2 s on average. Random simulation results for different cases are shown in Figure 3 and Figure 4.

3. Flow simulation results of two test cases of both scenarios

A single-phase fluid flow simulation is conducted for the two test cases in Figure 3 and Figure 4 of both scenarios. Related settings are described in Section 2.2 of this paper. Following Figure S4-1 and Figure S4-2 shows the simulated pressure maps after different days of flow simulation for the reference, 5 random GANSim-produced and 5 random SNESIM-produced geomodels of each test case.

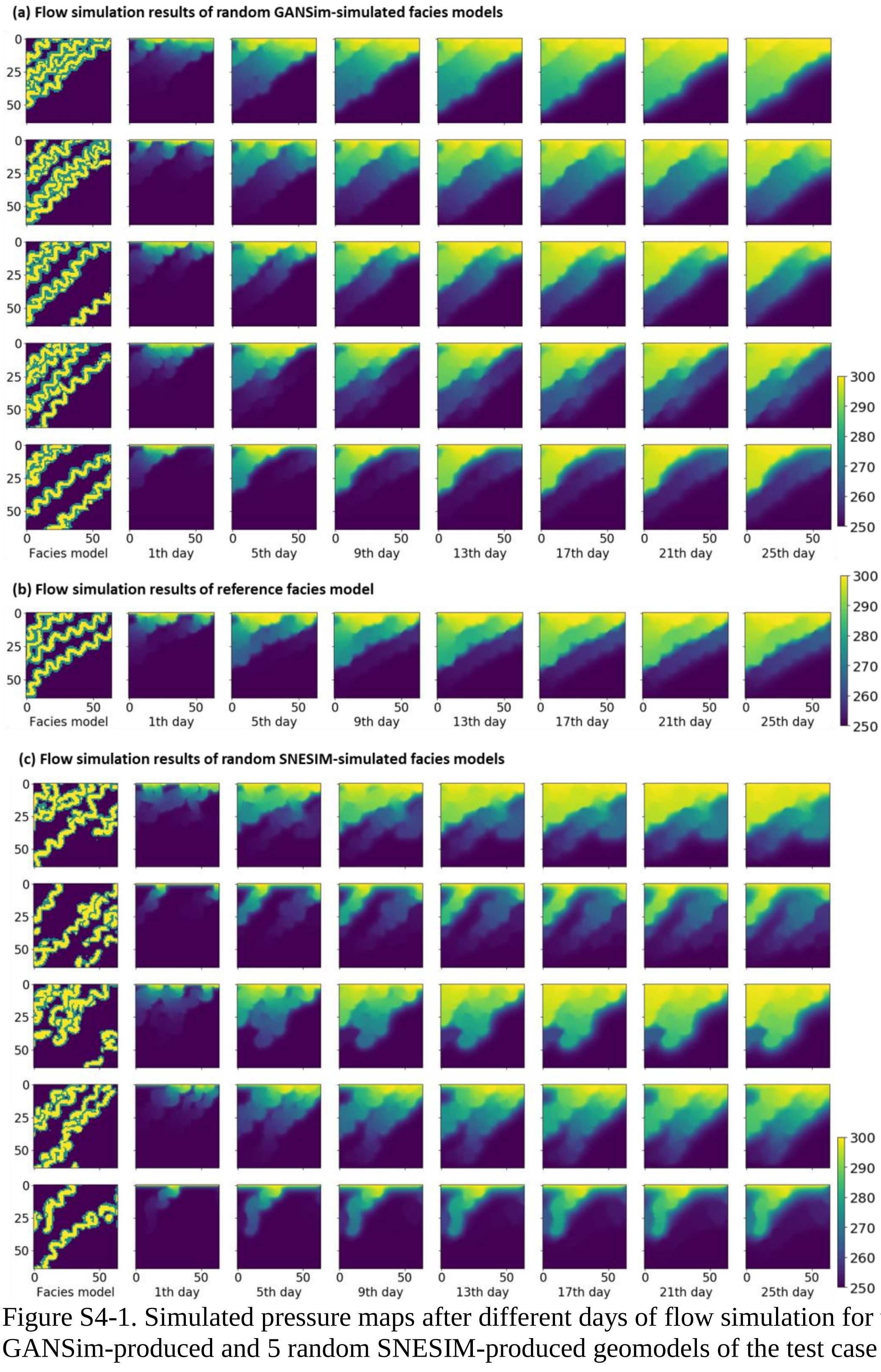

Figure S4-1. Simulated pressure maps after different days of flow simulation for the reference, 5 random GANSim-produced and 5 random SNESIM-produced geomodels of the test case in Figure 3.

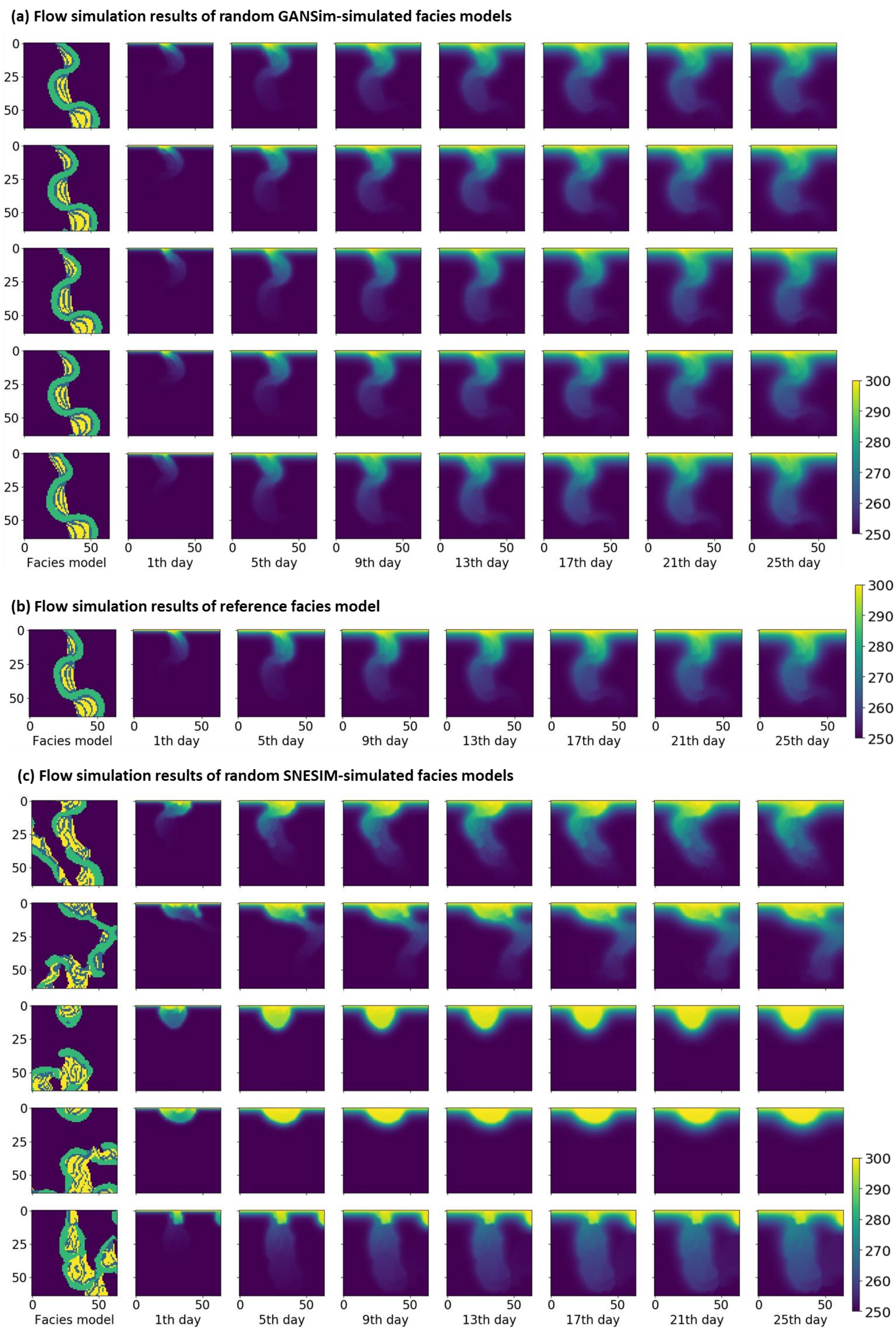

Figure S4-2. Simulated pressure maps after different days of flow simulation for the reference, 5 random GANSim-produced and 5 random SNESIM-produced geomodels of the test case in Figure 4.

References

Alqassab, H. M., Feng, M., Becker, J. A., Song, S., & Mukerji, T. (2024). MAGCS: Machine Assisted Geologic Carbon Storage (Vol. ADIPEC, p. D021S044R001). https://doi.org/10.2118/222120-MS

Gravey, M., & Mariethoz, G. (2020). QuickSampling v1.0: A robust and simplified pixel-based multiple-point simulation approach. *Geoscientific Model Development*. https://doi.org/10.5194/gmd-13-2611-2020

Gulrajani, I., Ahmed, F., Arjovsky, M., Dumoulin, V., & Courville, A. (2017). Improved training of Wasserstein GANs. In *In Proceedings of the 31st International Conference on Neural Information Processing Systems* (pp. 5769–5779).

Karras, T., Laine, S., & Aila, T. (2018). A Style-Based Generator Architecture for Generative Adversarial Networks. In *Proceedings of the IEEE/CVF Conference on Computer Vision and Pattern Recognition* (pp. 4401–4410).

Kingma, D., & Ba, J. (2014). Adam: a method for stochastic optimization. *arXiv Preprint*, arXiv:1412.6980. https://doi.org/10.1109/ICCE.2017.7889386

Mariethoz, G., Renard, P., & Straubhaar, J. (2010). The direct sampling method to perform multiple-point geostatistical simulations. *Water Resources Research*, *46*(11), 1–14. https://doi.org/10.1029/2008WR007621

Pyrcz, M. J., & Deutsch, C. V. (2014). *Geostatistical Reservoir Modeling* (2nd ed.). Oxford University Press.

Song, S., Mukerji, T., & Hou, J. (2021a). Geological Facies modeling based on progressive growing of generative adversarial networks (GANs). *Computational Geosciences*. https://doi.org/10.1007/s10596-021-10059-w

Song, S., Mukerji, T., & Hou, J. (2021b). GANSim: Conditional Facies Simulation Using an Improved Progressive Growing of Generative Adversarial Networks (GANs). *Mathematical Geosciences*. https://doi.org/10.1007/s11004-021-09934-0

Song, S., Mukerji, T., Hou, J., Zhang, D., & Lyu, X. (2022). GANSim-3D for Conditional Geomodeling: Theory and Field Application. *Water Resources Research*. https://doi.org/10.1029/2021WR031865

Strebelle, S. (2002). Conditional simulation of complex geological structures using multiple-point statistics. *Mathematical Geology*, *34*(1), 1–21. https://doi.org/10.1023/A:1014009426274

Song, S., Mukerji, T., Scheidt, C., Alqassab, H., & Feng, M., Geomodelling of multi-scenario non-stationary reservoirs with enhanced GANSim. Under review. 2025.